UNITED STATES
NAVAL POSTGRADUATE SCHOOL

A FEASIBILITY STUDY OF A METHOD TO
ANALYSE THE MOON'S SURFACE USING
NUCLEAR INELASTIC SCATTERING

* * * *

Robert J. Stinner

A FEASIBILITY STUDY OF A METHOD TO ANALYZE THE MOON'S SURFACE USING NUCLEAR INELASTIC SCATTERING

LT. Robert J. STINNER

11 May 1961

Submitted in partial fulfillment of the requirements for the degree of Master of Science. U. S. Naval Postgraduate School, Monterey, Calif.

UNIVERSITY OF CALIFORNIA
LAWRENCE RADIATION LABORATORY
LIVERMORE, CALIFORNIA

A FEASIBILITY STUDY OF A METHOD TO ANALYZE THE MOON'S SURFACE USING NUCLEAR INELASTIC SCATTERING

Robert J. Stinner

A FEASIBILITY STUDY OF A METHOD TO ANALYZE THE MOON'S SURFACE USING NUCLEAR INELASTIC SCATTERING

ABSTRACT

A selenological study by the Jet Propulsion Laboratory shows that the following elements could be found in abundance on the moon: Fe, Si, Mg, Al, O, K, Na, Ca, and Ni. An investigation was made to determine if the gamma rays produced by de-excitation of these nuclei, after the inelastically scattering of 14-Mev neutrons, could be used to determine the minimum abundance of various elements in a typical geological matrix. A general statement can be made that less than 1% by atom of Fe, Si, Mg, and Ni, and less than 4% of the remaining elements could be measured.

Inelastic (n,n') spectra are shown for each pure element and some excited state transitions not previously reported are suggested.

A FEASIBILITY STUDY OF A METHOD TO ANALYZE THE MOON'S SURFACE USING NUCLEAR INELASTIC SCATTERING

INTRODUCTION

When energetic neutrons are used to bombard samples of material, three nuclear processes can occur. These are (1) Elastic scattering; (2) Inelastic scattering[1]; (3) Capture and subsequent decay.

The usual sequence of events in the bombardment process is for the neutrons to make a number of elastic and inelastic collisions, losing energy with each collision. Each inelastic collision leaves a nucleus in an excited state. In order for the nucleus to de-excite to the ground state as quickly as possible, prompt gammas are emitted whose energy is uniquely related to the mode of de-excitation. When the neutrons reach thermal energies (~ .025 e.v.) capture takes place. If the capture process results in an excited state of the nuclide prompt gammas are emitted by a mechanism similar to that of the inelastic scattering. After a relatively long period, dependent on the half-life, the nuclide may decay emitting a beta, gamma ray, or both in the process. These gammas are known as activation gammas.

If one uses a pulsed neutron source and defines zero time at the beginning of each pulse then a time spectrum of the emitted gammas can be plotted. (See Figure 1). Three main features are readily apparent. Since the time of arrival of inelastic gammas is only dependent upon the travel time of the neutrons from the source to the target plus the travel time of

[1] This phenomenon actually results from a reaction process whereby a compound nucleus is formed. Competition sets in between different modes of decay. Because of the Coulomb barrier, the emission of neutrons is much more probable than the emission of charged particles. The re-emitted neutrons can leave the nucleus in an excited state, so that we obtain inelastic scattering. (n.b. El-53)

TABLE I.

ITEM	DEFINITION	FORMULA	POSSIBLE REACTIONS
Elastic Scattering	A collision process in which kinetic energy is conserved.	$X + x \rightarrow X + x$	(n,n) (p,p) (d,d) etc.
Inelastic Scattering	A collision process in which kinetic energy is not conserved. The gamma rays are known as inelastically produced gamma rays.	$X + x \rightarrow X^* + x'$ $\hookrightarrow X + \gamma$'s	(n,n')
Radiative Capture	A capture process which leaves the product nucleus in one of its excited levels. The nucleus de-excites promptly emitting gammas. These gammas are known as radiative capture gammas.	$X + x \rightarrow Y^*$ $\hookrightarrow Y + \gamma$'s	(n,γ) (p,γ)
Radioactive Decay	The decay of an unstable nucleus to a daughter product by β-decay. The product nucleus may be in an excited state which de-excites promptly emitting gammas. These gammas are known as activation gammas.	$X \rightarrow Y + \beta$ $X \rightarrow Y^* + \beta$ $\hookrightarrow Y + \gamma$'s	(p,β) (n,β)

the gammas from the target to the detector a sharp peak will be noted whose distance from the origin is equal to the above time sum and whose width is of the order of the neutron pulse width. After formation of the inelastically produced gamma rays the neutrons continue to lose energy until thermalized and are captured. This normally requires 10 - 1000 microseconds. Therefore the resulting radiative capture gammas appear as a broad peak extending over this time range. Finally, there is a low steady state level which tends to raise the two peaks. This "background" is due to: (1) Natural activity of the experimental environment; (2) Remainder of the radiative capture counts left over from the previous pulse; (3) Activity resulting from the decay of the radionuclides formed in the bombardment process. By gating a pulse height analyzer so that only the counts of the inelastic peak (plus a few background counts) are analyzed it is possible to obtain a spectrum whose peaks are indicative of the nuclear levels of the isotope being bombarded.

During the past years, considerable work (Da-56, Sc-57, et al) has been done in determining the cross-section for (n,n') reactions for various elements using pulsed neutron sources and time-of-flight techniques. It has been noted that the various common isotopes differ markedly in their principal level structure, but have quite similar excitation cross-sections. This feature led Dr. Carlton Schrader and E. F. Martina (Sc-60) to conclude that since one could determine the presence of an unknown level in a known isotope by (n,n') reactions then conversely one could determine the presence of an unknown isotope by interpreting a spectrum of gamma rays from levels in an unknown sample. Furthermore, since the reaction cross-sections were similar, it should be possible to determine the isotopes present and their relative abundances in the unknown mix. If the conclusions

were correct remote analysis of material would be possible. In particular, a payload could be designed to sample the moon's surface and deduce the elements present. Based on this line of reasoning, a study was begun of the feasibility of using inelastic scattering techniques to determine the composition of the moon's surface. Four questions were to be answered:

1) Can the energy levels of the likely constituents be resolved by simple methods?

2) Do the isotopic energy levels have relatively similar inelastic cross-sections?

3) What minimum abundances could be determined?

4) With what precision could these abundances be stated?

THE MOON

The moon, our first satellite, has been a subject of conjecture since man first raised his eyes to the night sky. Only recently, however, has conjecture been augmented by scientific analysis and experimentation. While it is possible to formulate reasonable theories concerning the origin and physical composition of the moon using telescopes, spectroscopes, radar and other observation tools, the advent of the space age now permits physical testing of the validity of these theories.

The oldest theory of the moon's formation was proposed philosophically by Kant and scientifically by LaPlace. Known as the "accretion theory", it proposed that a slowly rotating equatorial ring of gas and dust coalesced into a single satellite whose size approximated the moon's size as we know it today. This theory closely parallels the accretion theory of the formation of the solar system. The accreted mass heated up causing partial melting with the escape of large quantities of steam and other gases. Subsurface explosions occurred producing funnel-shaped craters (pre-mare). Later, lava flows covered much of the surface. Cooling and solidification

of the interior then took place. Impacting meteorites formed the post-mare craters strewing granitic and meteoritic rubble in great ray systems over the surface of the moon. The process was completed prior to 10^9 years ago.

The second theory of formation is a fairly recent one proposed by George Darwin in the late 19th century. In a study of tides and their effects, Darwin noted that early in geologic history, the earth's daily rotation of four hours coupled with the sun's gravitational attraction produced tidal effects every two hours which coincided with the earth's natural vibratory period of two hours. From this, he postulated that resonances were set up and a large tidal bulge appeared on the surface. Fission occurred, a moon was formed and the Pacific Ocean basin was left as a testimonial to the event.

Since this could occur only to a plastic sphere (Darwin assumed a liquid earth), isostatic readjustments would take place both on the earth and the moon. (Splitting of the Americas from the Eur-African land mass and formation of the Atlantic Ocean basin was proposed as the earth's adjustment.) On the moon, one would expect a rather thick granitic crust overlying a basaltic core. A cool core would not be likely. Continued volcanism and extensive lava beds would be present.

The latest theory pictures the formation of the moon as an independent event. At some time during the ages this "meteorite" passed close to the earth and was captured in a slightly elliptical orbit. If this is so, then one would expect a typical meteoritic type surface.

The above listing of possible origins of the moon permits one to make various postulates in regard to the moon's surface. One such analysis by Jet Propulsion Laboratory (Me-60) is shown in Table III. We expect that the most abundant elements would be Iron, Silicon, Magnesium, Aluminum, Oxygen, and Calcium. Potassium, Sodium and Nickel might also be present.

TABLE II. THE FORMATION OF THE MOON

THEORY	METHOD	COMPOSITION OF THE MOON
Accretion	Slowly rotating mass of gas and dust coalesced into a single satellite. Subsequent heating produced funnel-type craters and permitted large lava flows. Cooling of interior then occurred.	Basaltic Marias. Granitic uplands. Majority of craters impact type. Pumice expelled from craters composed of granitic and meteoritic material.
Fission	Tidal resonance due to matching of plastic earth's rotational period and natural vibratory period caused large mass to be torn from the earth. Generally proposed that this mass came from Pacific Basin. Hot core remains.	Granitic crust. Basaltic interior. Large basaltic lava flows appear on crust.
Capture	Moon formed as independent event outside influence of earth's gravitational field. During passage through space passed close to earth and captured by gravitational field.	Meteoritic type composition.

(Abundant Nickel would be found only in meteoritic debris.) Furthermore the relative amounts of the elements would depend upon the geologic type of surface so that the ratio of abundance of one element to another would be an indicator of the method of moon formation.

TABLE III. SELENOLOGICALLY IMPORTANT ELEMENTS (after JPL)

Element	Concentration (% by weight)	
	Low	High
Fe	1.5	15*
Si	15.0	35
Mg	0.2	22
Al	0.5	12
O	40.0	48
K	0.1	6
Ca	0.5	12
Na	0.2	7
Ni	0.002	9

* Iron - nickel meteorites will contain 90% iron.

EXPERIMENTAL

A. Ring Procedure

Having decided which elements were of interest, work was begun to obtain representative spectra so that the principal energy levels could be determined. A time-of-flight technique first developed at this laboratory (Be-59) was used. A diagram and photograph of the experimental set-up are shown in Figures 2 and 3.

Deuterons, injected into a 350 kev Cockcroft-Walton machine, were accelerated, swept, and bunched; then deflected onto a thin (0.1 mil)tritium occluded titanium target. Short bursts (about 3×10^{-9} seconds) of 14-Mev

neutrons were produced by the reaction

$$_1D^2 + _1T^3 \rightarrow {}_2He^4 + {}_0n^1 + 17.3 \text{ Mev}$$

at a repetition rate of 5 mc/sec. The neutron flux (about 300 neutrons/pulse) was monitored by counting the alpha particles in a gas proportional counter mounted in a position 174° with respect to the ion beam. Thin rings were placed so that there was a 70° angle between the incident neutrons and the detected gamma radiation thereby neutralizing the anistropy of the radiation. A copper attenuator was placed in the line-of-sight of the target and detector so that neutron activation of the scintillator would be minimized. The gamma detector, consisting of a cylindrical 1-3/4" diameter x 2" NaI (Tl) crystal mounted on an RCA-6810A photomultiplier tube, was placed in a lead housing whose walls were 4" thick. Refrigeration coils encircling the housing maintained the photomultiplier and crystal at a constant temperature ($16^\circ C$) so that temperature dependent gain variations were eliminated.

The detector-analyzer system was divided into a fast channel circuit and a slow channel circuit (Fig. 4). The fast signal, taken from the anode of the photomultiplier, was amplified and used to start the time-to-height converter. The regularly repeating pulse made by the deuterons striking the target was delayed, amplified and used to stop the time-to-height converter. The converter produced a voltage which was proportional to the time difference between the arrival of the start and stop pulses. By setting the differential discriminator for specific voltage ranges, gates would be generated for viewing only those gammas which satisfied a particular time relationship with respect to the neutron burst. The slow signal, take from the 9th dynode, was suitably delayed, linearly amplified and analyzed by the gated 256-channel pulse height analyzer.

The lower trigger level on the analyzer was set so that protons of less than 225 kev were not analyzed. In order to account for the effect of this discrimination on the dead time calculations, an integral discriminator and associated scaler were included in the slow circuit. A switching and coincidence control was used to display either the time spectrum or gated time spectrum to facilitate setting the differential discriminator. A third position on the control was used for the run.

Scalers at various points in the circuit were used to count start, slow, and gate pulses. The analyzer also had a scaler output indicating dead time within the analyzer, and this, plus the information from the other scalers was used to compute the dead time of the total system.

A run was made with the rings in place to obtain a "signal plus background" spectrum and with the ring removed to obtain a "background" spectrum. For each run except Oxygen, 2.5×10^{11} neutrons were produced. Because of Oxygen's low inelastic cross-section and the desire to reduce statistical variation of the triple peak 5×10^{11} neutrons were used in the run. After the run was completed, the analyzer information was printed out on paper tape and the scalers and elapsed time were recorded. This information was transferred to punched IBM cards. An IBM 650 computer was programmed to compute the Dead Time Correction; apply it to both the "background" and "signal plus background" information; subtract the "background" from the "signal plus background" and print out the corrected signal.

The "Dead Time Correction" was a multiplicative factor determined by the computer solution to the equation:

$$D.T.C. = 1 + 60/T \left[Nd/60 - 2 \times 10^{-6} Nc + 3.5 \times 10^{-6} Ni + 1.0 \times 10^{-6} Ns \right]$$

where T = Run duration time in minutes

Nd = Number of counts registered in the pulse height analyzer dead time monitor.

Nc = Total number of counts in the memory core of the pulse height analyzer.

Ns = Number of start pulses to the time-to-height converter.

Ni = Number of slow pulses appearing at the input to the pulse height analyzer.

The constants were determined empirically by measuring the dead times of the various electronic components. (A thorough discussion of this analysis is contained in Appendix II of UCRL 5596 (Be-59)).

The printouts from the IBM 650 computer were plotted on rectangular graph paper. The various spectra are shown in Figs. 7-15. From these the most prominent peak of each element was selected and the number of inelastic gammas contributing to this peak were counted. This count was compared to the number of counts in the $Fe_{0.84}$ peak and a "Minimum Abundance Factor" (F) was defined and computed using the following equation. (See Appendix for derivation and definition of terms):

$$F = \frac{G_x}{G_{0.84}} \times \frac{N_{Fe}}{N_x} \times \frac{(\cos\phi_1 - \cos\phi_2)_{Fe}}{(\cos\phi_1 - \cos\phi_2)_x} \times \frac{(r_2 - r_1)_x}{(r_2 - r_1)_{Fe}} \times \frac{A_{t_x}}{A_{t_{Fe}}} \times \frac{M_{Fe}}{M_x}$$

It is assumed that isotopic abundances in a particular element would be the same on the moon so that this term is neglected. Since Iron was assigned the arbitrary value of 1 the solution of the equation gave an indication of the likelihood of noting the presence of an element as compared to Iron.

B. Sand Matrix Geometry

If gamma particles are formed deep in a formation, there will be a certain percentage absorbed in their passage out of the formation to the detector. The percentage is dependent upon the absorption cross-section which in turn is dependent upon three principal effects: 1) the photoelectric effect: The incident gamma particle is absorbed and another particle

(usually a K-shell electron) is ejected leaving the atom in an excited state; 2) pair production: The gamma particle is acted upon by the coulomb field of the nucleus forming an electron-positron pair. Annihilation of the positron occurs and two 0.51 Mev photons are emitted in opposite directions and with opposite polarizations. The threshold for this reaction is 1.02 Mev with the pair acquiring the remaining energy. (It is possible for one or both of the 0.51 Mev gammas to be detected at the same time that the resultant photopeak is being detected so that it appears that the original gamma ray was reduced by only 0.51 Mev or not at all.) 3) Compton effect: The gamma particle collides with an orbital electron and, depending upon the angle of the collision, loses only a portion of its energy. A broad, continuous spectrum of energies up to the Compton edge results.

Since these same phenomena also occur in the crystal, it was feared that the total effect of the energy degradation would be large enough to swamp the characteristic inelastic peaks. Because of this and also to determine the minimum amount of Iron, Magnesium, and Aluminum that could be detected it was decided to mock-up a formation whose three dimensions were greater than several mean free paths of a 14-Mev neutron. Any terrestrial abundance table one uses lists Oxygen and Silicon as the most common elements by far. With this in mind, 1800 lbs. of a granitic-type sand was used as the carrier for the varying amounts of Fe, Mg, and Al.

TABLE IV. Atomic Composition of Carrier Sandpile

Element	Percentage by Atoms
Oxygen	64.6
Silicon	26.7
Aluminum	5.7
Potassium	1.6
Iron	0.6
Calcium	0.5
Trace	0.3

The sand was placed in a 5' x 5' x 1-1/2' wooden box whose upper level was located 4" below the neutron source. The detector and its housing was suspended 4-1/2' above the source. (See Fig. 5 and 6).

The detection-analyzing system was identical to the Ring phase of the experiment. Operating procedures were also identical except for one notable exception. For the "signal plus background" run the gating system was set on the inelastic gamma peak of the time spectrum as was done for the rings. However, since it would not be possible to remove the formation for background measurements, the gate was delayed in time so that those counts arriving just after the peak would be analyzed. Since the activation gamma spectrum is nearly constant the same gate width was used so that the measured background was very nearly equal to the background contributing to the inelastic gamma peak.

Prior to varying the composition of the sand, runs were made at each of two different energy band widths (0-3 Mev and 0-8 Mev) to obtain representative spectra. The various elements of interest (Fe, Mg, and Al) were then added separately in increasing percentages with runs being made after each increase. The recorded data, consisting of "signal plus background", "background" and scaler readings was transferred to IBM cards and processed as before.

The printouts from the formation experiments were plotted on rectangular graph paper as before. However, to illustrate to the reader the growth of a peak as the elemental percentage was increased, the formation curves for a particular element were normalized and superimposed. As was pointed out earlier, Silicon is a very abundant element in all terrestrial and meteoritic material. Furthermore, since Iron, Aluminum, and Magnesium had prominent energy peaks less than 2.5 Mev, it was decided to use the 1.78 Mev peak of Silicon as a base for determining the calibration

and precision of the experiment. The formation spectra were analyzed in the following manner:

1) A line representing the best estimate of the Compton scattered continuum was drawn under the $Si_{1.78}$ peak and under the element peak in question.

2) The number of gammas contained in each peak were counted.

3) A ratio of the counts in the peak in question to the counts in the $Si_{1.78}$ peak was formed ($Cx/C_{1.78}$). This ratio was used as an abscissa value on a calibration curve.

4) Since the number of atoms of each element used was known, a ratio of the number of atoms of the element under question to the number of atoms of Silicon was formed (Nx/N_{Si}). This ratio was used as the ordinate of the calibration curve.

The calibration curves for Fe, Al, and Mg are shown in Figs. 19, 21 and 23. The percentages in the parentheses are the uncertainty in measuring the area of each peak. This uncertainty is due to both the Compton continuum subtraction and the unfolding of contributions by other elements to the peak in question.

RESULTS

1. Iron (Fig. 7.)

The line at 0.84 Mev represents a transition from the 2^+ first level of Fe^{56}. Since apparently all cascades from higher levels pass through this state, the intensity is not surprising. The formation spectra (Fig.18) show that a 1% abundance increase added about 5,000 counts to the 0.84 peak. It would not be unreasonable to expect to detect a 500 count peak at this energy level so that one can conclude that a minimum abundance of 0.1% of Fe would be detected.

2. Silicon

The gamma ray at 1.78 Mev is the first level (2^+) transition of Si^{28}. The peak contains upwards of 8,000 counts. Relating this to the 62,900 counts of $Fe_{0.84}$ for the same number of neutrons, the Minimum Abundance Factor was 0.212 so that an abundance of 0.5% should be detected.

The other peaks shown in Fig. 8, are due to transitions in Si^{29}.

3. Magnesium

The first excited level of Mg^{24} is at 1.37 Mev (2^+) and produces the intense peak seen in Fig. 9. In addition peaks are found at 0.88 Mev and 1.82 Mev and are due to the 5.1 → 4.2 Mev Mg^{24} transition and Mg^{26} first level transition respectively. The principal peak count was 25,900, giving an "F" value of .342 so that a 0.3% abundance should be detected. This is confirmed by the formation spectra where a 1% increase in abundance added 1,700 counts to the 1.37 peak (Fig. 20).

In the actual analysis, the 1.37 peak is smeared by the contribution of the abundant Si^{29} 1.28 Mev peak. Standard procedure would be to take the spectrum of Si alone (obtained from the ring experiments), and, using a computer, normalize to the prominent 1.78 Mev peak and subtract the entire $Si_{1.28}$ contribution.

4. Aluminum

The inelastic scattering of 14-Mev neutrons from Al^{27} produced 1.01-, 1.77-, and 2.20-Mev gamma rays (Fig. 10). It has been concluded by all investigators that the 1.01- and 2.20-Mev gamma rays are produced by second and third excited state transitions to the ground state respectively. The 1.77-Mev gamma ray has been suggested by Morgan (Mo-56) to be due to a 2.73 → 1.01-Mev transition. However, the broadness of the base and the lack of symmetry of the photopeak suggests additional con-

tribution. It is proposed that there is both a 1.96-Mev gamma ray from a 2.97 → 1.01 Mev transition (Nuclear Data Card Scheme) plus the 2.20-Mev photopeak Compton edge enhancement.

No evidence was found for a 0.84-Mev gamma ray but the photopeak was probably masked by the Compton edge of the 1.01-Mev gamma ray.

The 1.01-Mev photopeak, because of its abundant count, would be ideal for calibration purposes. However, if a large amount of Silicon is present the Si^{29} 0.98 gamma ray will mask the Al contribution. Therefore, the 2.20-Mev transition was used for calibration. There were 8,700 counts and the "F" factor was 0.047 indicating a minimum amount detectable of 2%. From the formation spectra a 2% increase in Al added 540 counts to the 2.20-Mev photopeak, thereby confirming the calculation.

5. Oxygen

Experimental results up to 1959 on the O^{16} nucleus have been summarized by Ajzenberg and Lauritsen (AJ-59). The doubly-magic configuration of this nucleus predicts a first level of zero spin and even parity. Decay is by emission of nuclear pairs. The 6.14-Mev second excited state to ground transition with its associated pair (5.12 Mev) and pair plus one (5.63 Mev) energy peaks is observed. Four other peaks are noted and assigned as follows:

E_γ (Mev)	Transition
3.65	9.84 → 6.14
2.73	8.87 → 6.14
2.22	11.08 → 8.87
1.95	8.87 → 6.91
1.72	8.87 → 7.12

With the exception of O^{16}, none of the logical target elements have abundant transition energies in excess of 4.5-Mev. Therefore, the O^{16} triple peak (5.12, 5.63, 6.14 Mev) is easily recognized. This bombardment produced 17,000 counts in this triplet for double the usual number of neutrons (5×10^{11}). However, since a triplet is used and since the resolution of the detection system increases the base length of the peak at higher energies, the minimum acceptable and detectable number of counts was increased by an order of magnitude. With this adjusted number of counts the computed minimum abundance was 3.7% and, indeed, is well below the expected minimum lunar abundance.

6. Potassium

Very little (n,n') experimentation on the stable isotopes K^{39} (93%) and K^{41} (6%) has been reported in the literature. A Los Alamos group (Li-57) noted levels at 2.52-, 2.81-, 3.05-, and 3.59-Mev representing the first four excited states of K^{39}.

Bombardment of natural Potassium by 14-Mev neutrons for this experiment produced 2.52-, 2.81-, and 4.10-Mev gamma rays; believed to be predominately direct transitions from the associated level to the ground level of K^{39} (Fig. 12. insert). A strong photopeak was observed at 2.15-Mev and is assigned to a K^{39} 4.68 → 2.53-Mev transition. The 0.78-Mev gamma ray is assigned to the de-exciting of the fourth level of K^{39} (3.60-Mev) via the second level (2.82-Mev). There was no indication of (n,n') scattering by K^{41} (isotopic abundance 6.91%).

The 2.15 Mev photopeak contained 6,000 counts, giving F = 0.10 so that 1% of Potassium would be detected. If Al is present in sizeable amounts (>1%), as is usually the case, the peak would be enhanced but an unfolding by a computer would resolve the various contributions.

7. Calcium (Fig. 13)

The principal Calcium isotope, Ca^{40} (97%), like O^{16} is a double-magic nucleus. Therefore transitions from the first excited level (3.35-Mev) can only occur by nuclear pair emission. This is confirmed by the intensity of the annihilation radiation (0.51-Mev). The number of lower energy transitions (0.77-, 0.89-, 1.16-Mev) is surprising but the spectrum is similar to that reported by R. B. Day (Da-56) who attributes the first two energies to (n,p',γ) K^{40} reactions and the last energy to a Ca^{44} first level de-excitation. A fourth peak, not previously reported as of 1959, appears at 1.64-Mev and agrees remarkably well with the 1.639-Mev fourth excited state of K^{40}.

The 0.77 gamma ray peak, containing 13,000 counts was selected for the minimum abundance factor calculation. These are sufficient counts to expect a minimum of 1.2% Ca would be detected. However, Fe is usually found when Ca is present so that the $Fe_{0.84}$ and $Ca_{0.77}$ would merge and a computer solution similar to that outlined for Magnesium would be necessary.

8. Sodium

Previous (n,n') investigators (Mo-56, and others) of Na^{23}, the only stable Sodium isotope, have reported 0.44-, 0.61-, and 1.64-Mev gamma rays. Two other gamma rays were observed (Fig. 14) to which logical transitions can be assigned:

E_γ (Mev)	Transition
0.99	3.68 → 2.70 Mev
1.29	3.68 → 2.39 Mev

Since many higher levels often decay via the Na^{23} first level, the 0.44 peak is intense and, indeed, screens from observation the 0.51 annihilation peak. Because of this eclipse, the 0.63-Mev peak was used to

compute the minimum detectable abundance of 1.3%. However, in most rock types, when abundant Na is found abundant K is also found, and since the isotope K^{39} has its principal peak near this energy (0.65-Mev) reinforcement would take place. The exact Na abundance would then be obtained by using the 1.29-Mev peak after unfolding the contribution of $Si_{1.28}$ and other elements.

9. Nickel (Fig. 15)

Natural Ni has two abundant isotopes, Ni^{58} (67.8%) and Ni^{60} (26.2%), both of which contribute significantly to the inelastic spectrum. The 1.01-, 1.33-, and 1.45-Mev inelastic gamma rays have been observed and reported by others (Ki-54 , Da-56 , Si-56). The remaining energies are tentatively assigned as follows.

E_γ (Mev)	Transition	Isotope
0.44	2.90 → 2.46 Mev	Ni^{58}
0.65	3.42 → 2.77 Mev	Ni^{58}
1.17	2.50 → 1.33 Mev	Ni^{60}

No peak was observed at 0.83 Mev (Da-56) but this energy was probably masked by the 1.01-Mev gamma ray Compton edge.

The most suitable energy for detecting Ni would be the first excited state transition of Ni^{58} (1.45 Mev) since this is well separated from the 1.30 and 1.80 energies of Si, Mg, and Fe. From the counts in the peak, 1% Ni should be detected (F = 0.11). However, such abundant nickel would only be present if considerable amounts of Iron-Nickel meteoritic debris were scattered about, so that the appearance of nickel's characteristic energies in the inelastic spectrum would be strong evidence for lunar crater formation by meteorites.

CONCLUSIONS

The remote analysis of the lunar surface by neutron-gamma inelastic scattering techniques is feasible. Examination of the pure inelastic spectra (Figs. 7-15) shows that, in general, the predominant photopeak of a particular element has a unique energy when compared to the prominent photopeaks of the other abundant elements. Furthermore, after normalizing these spectra (as part of the "Minimum Abundance Factor" calculation) the counts in each prominent peak were equal within an order of magnitude, and therefore the inelastic cross sections for the production of these gamma rays are comparable.

The minimum abundances that could be detected varied from 0.1% for Iron to 3.7% for Oxygen. A summary is shown in Table V. Abundance measurement precisions have been determined for Fe, Mg, and Al. Since these values are dependent on Compton continuum base line selection and spectra unfolding techniques, the point of interest on the particular calibration curve should be consulted.

ACKNOWLEDGMENTS

I am grateful for the purpose and direction shown by Dr. Carlton D. Schrader without whose supervision and advice this work could not have been done, and to Dr. Hans Mark whose continuing enthusiasm and interest was a source of inspiration. I am indebted to Messrs. Bernard Hoop, Constantine Chelly and Arthur Williams who assisted during different phases of the study and especially to Douglas McMillin who programmed the IBM 650 computations. Particular mention should be made of Mrs. Joanna Phifer who prepared the various figures and samples. Finally, I would like to express my gratitude to Chief Operator Roy V. Cedarlund and his able assistants who so competently operated the Cockcroft-Walton Accelerator.

TABLE V. SUMMARY

Likely Elements to be Found on the Surface of the Moon	Principal Isotope	Isotopic Abundance	Prominent Energy Level	Minimum Detectable Abundance
Iron	Fe^{56}	91.5%	0.84 Mev	0.1%
Silicon	Si^{28}	92.3	1.78	0.5
Magnesium	Mg^{24}	78.6	1.37	0.3
Aluminum	Al^{27}	100.	2.20	2.0
Oxygen	O^{16}	99.8	6.14 (triple peak)	3.7
Potassium	K^{39}	93.	2.15	1.0
Calcium	Ca^{40}	97.	0.77	1.2
Sodium	Na^{23}	100.	0.63	1.3
Nickel	Ni^{58}	67.8	1.45	1.0

BIBLIOGRAPHY

(Aj-59) F. Ajzenberg-Selove, T. Lauritsen, Nuclear Levels of Light Nuclei, VI, North Holland Publishing Company, Amsterdam, 1959.

(Be-59) J. Benveniste, A. C. Mitchell, C. D. Schrader, J. H. Zenger, Lawrence Radiation Laboratory, University of California, Report UCRL-5596, June, 1959.

(Bl-53) J. M. Blatt, V. F. Weisskopf, Theoretical Nuclear Physics, John Wiley and Sons, New York, 1952, pg. 400.

(Da-56) R. B. Day, Phys. Rev. 102, 767.

(Ki-54) R. M. Kiehn, C. Goodman, Phys. Rev. 95, 989.

(Li-57) D. A. Lind, R. B. Day, R. M. Kloepper, Bull. Am. Phys. Soc. 2 No. 6, 309, H5, 1957.

(Me-60) A. E. Metzger, Jet Propulsion Laboratories, private communication.

(Mo-56) I. L. Morgan, Phys. Rev. 103, 1031 (1956).

(Sc-57) C. D. Schrader, J. Benveniste, J. H. Zenger, Bull. Am. Phys. Soc. 2, 309, 1957.

(Sc-60) C. D. Schrader, E. F. Martina, Lawrence Radiation Laboratory, University of California Report UCRL-5916, April 1960.

(Si-56) R. M. Sinclair, Phys. Rev. 102, 461.

APPENDIX

DEVELOPMENT OF THE MINIMUM ABUNDANCE FACTOR

Since it is not convenient to do a formation experiment for all elements of interest, a minimum abundance factor (f) was derived to provide a rough approximation of the minimum abundance that could be detected in a formation using the results of the ring geometry.

Three assumptions are made:

1) The neutron distribution is isotropic.

2) Multiple scattering is negligible.

3) The resultant gamma distribution is isotropic.

Select r_1 and r_2 so that the area of the included band equals the area of the ring cross-section and that the average radius $\frac{r_1 + r_2}{2}$ equals the distance from the origin to the midpoint of the diagonal of the ring cross-section.

Thus:

$$\frac{r_2^2}{2}\left[\phi_2 - \phi_1\right] - \frac{r_1^2}{2}\left[\phi_2 - \phi_1\right] = \tfrac{1}{4}\, a\, b \qquad (1)$$

and

$$\frac{r_2 + r_1}{2} = \left[R^2 + D^2\right]^{1/2} \qquad (2)$$

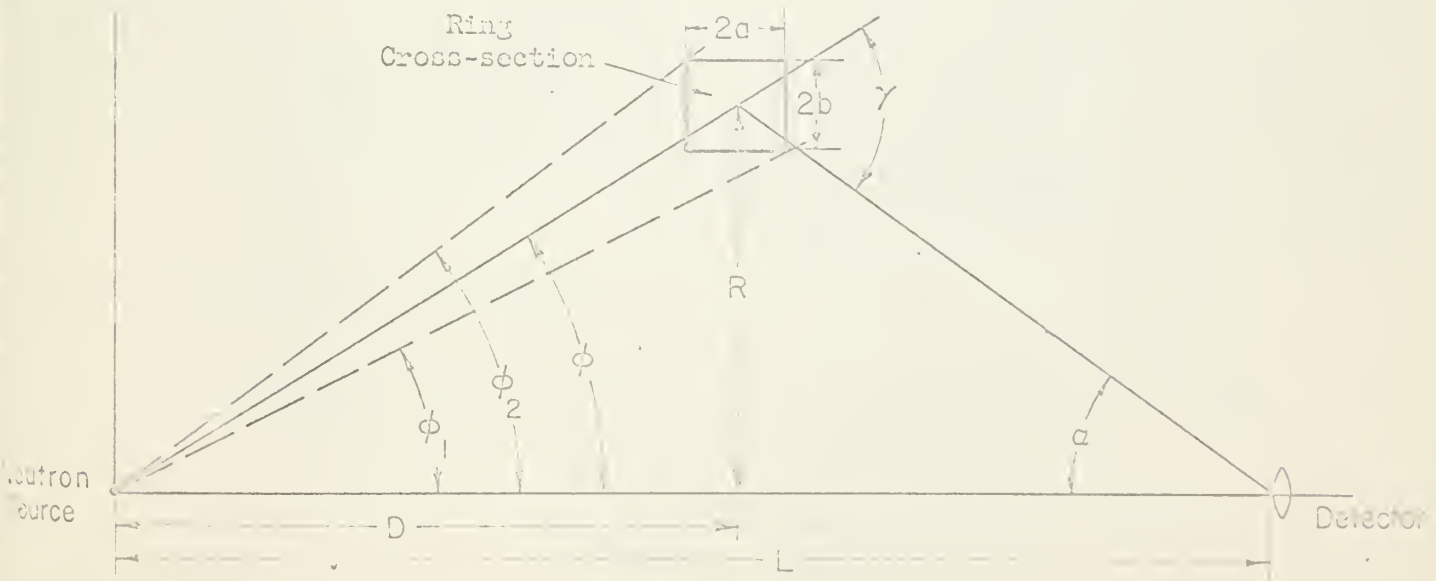

Obviously

$$\phi_2 = \tan^{-1} \frac{R + b}{D - a} \quad \text{and} \quad \phi_1 = \tan^{-1} \frac{b - R}{D + a} \tag{3}$$

so that

$$r_2 - r_1 = \frac{4 a b}{(R^2 + D^2)^{1/2}} \times \frac{1}{\phi_2 - \phi_1} \tag{4}$$

Since

$$\gamma = \phi + \alpha$$

$$\tan \gamma = \tan (\phi + \alpha) = \frac{\tan \phi + \tan \alpha}{1 - \tan \phi \tan \alpha} \tag{5}$$

or

$$\text{Tan } \gamma = \frac{\frac{R}{D} + \frac{R}{L - D}}{1 - R^2/D (L - D)} \tag{6}$$

Solving for D

$$D = \frac{L}{2} \left[1 - \left(1 - \frac{4 R^2}{L^2} (1 + L/R \tan \gamma) \right)^{1/2} \right] \tag{7}$$

The fractional solid angle (f) intersected by the ring on the neutron sphere is

$$f = \frac{d\Omega_1}{4\pi} = \frac{dA}{4\pi r^2} = \frac{\int_{\phi_1}^{\phi_2} \int_0^{2\pi} r^2 \sin\phi \, d\phi \, d\theta}{4\pi r^2} \tag{8}$$

Then, carrying out the integration

$$f = \frac{1}{2} \left[\cos \phi_1 - \cos \phi_2 \right] \tag{9}$$

the probability that a neutron will be scattered inelastically through a particular nuclear level while passing through the ring is

$$P = \sigma N_a \qquad \text{where: } \sigma = \text{inelastic cross-section of the level} \qquad (10)$$

N_a = Atomic surface density

but

$$N_a = \frac{M}{A_t} \frac{A_0}{r_2 - r_1} \qquad \text{where: } M = \text{mass of the element} \qquad (11)$$

A_t = Atomic weight

A_0 = Avogadro's number

So that the number of inelastic gammas of a particular energy that are formed is given by eqs. (9), (10), and (11).

$$G = Pf N = \frac{N}{2} \left(\cos\phi_1 - \cos\phi_2\right) \frac{\sigma M}{r_2 - r_1} \times \frac{A_0}{A_t} \qquad (12)$$

where: N = number of neutrons produced

The number of gammas that appear at the detector is a function of the average solid angle of the detector ($\overline{d\Omega_2}$) and is dependent upon the ring diameter and the distance from the ring to the detector. (This distance is also dependent upon the ring diameter). However, the diameter variations were small in comparison to ring-detector distance so that the respective $\overline{d\Omega_2}$ were considered equal.

The number of gammas, of a particular energy striking a crystal, that will be detected is dependent upon the size and efficiency of the crystal. Since the same crystal type and size would be used in the payload, these effects were neglected. Therefore, the number of counts in the photopeak: $\sim G$

The relative minimum detectable power can then be obtained as

$$r = \frac{c_1}{c_2} = \frac{C_1}{C_2} \times \frac{N_2}{N_1} \frac{\left(\cos \phi_2 - \cos \phi_3\right)_2}{\left(\cos \phi_1 - \cos \phi_2\right)_1} \frac{\left(r_3 - r_1\right)_1}{\left(r_2 - r_1\right)_2} \times \frac{\lambda_{o_1}}{\lambda_{o_2}} \frac{\nu_2}{\nu_1} \qquad (1)$$

where C = constant in the selected photopeak

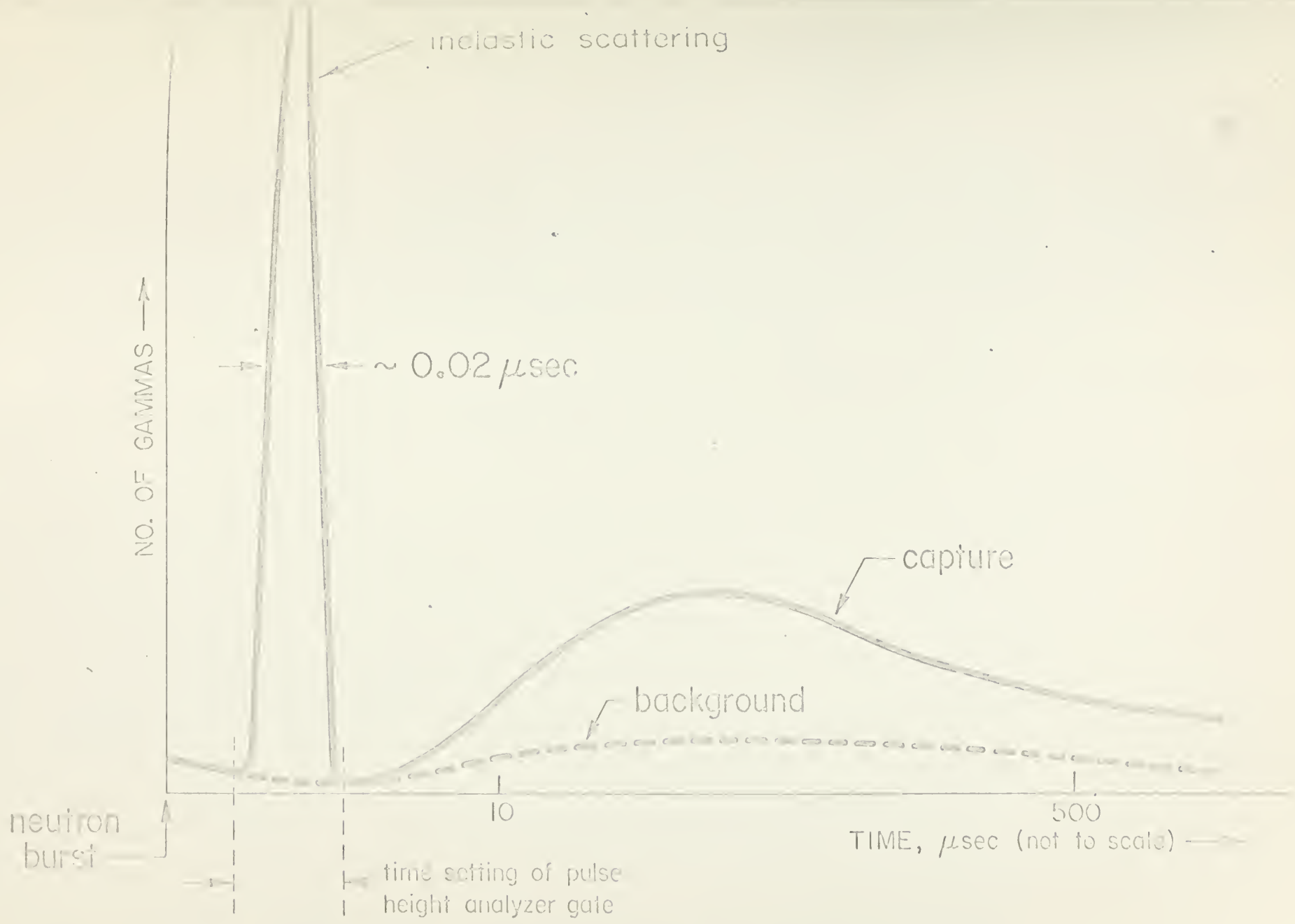

Fig. 1. Time Spectra


BEAM
PIPE
LEAD
HOUSING
ASSEMBLY

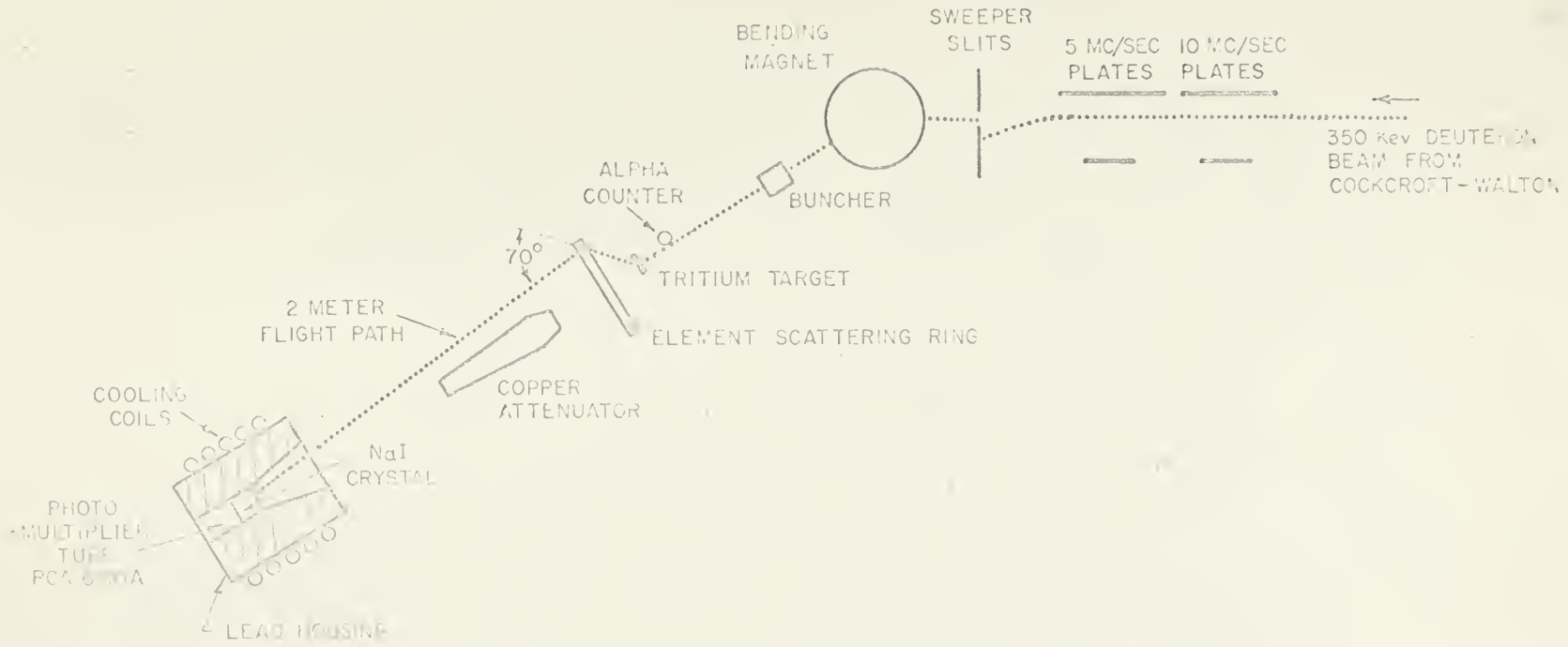

Fig. 3. Block diagram of "Ring" experiment.

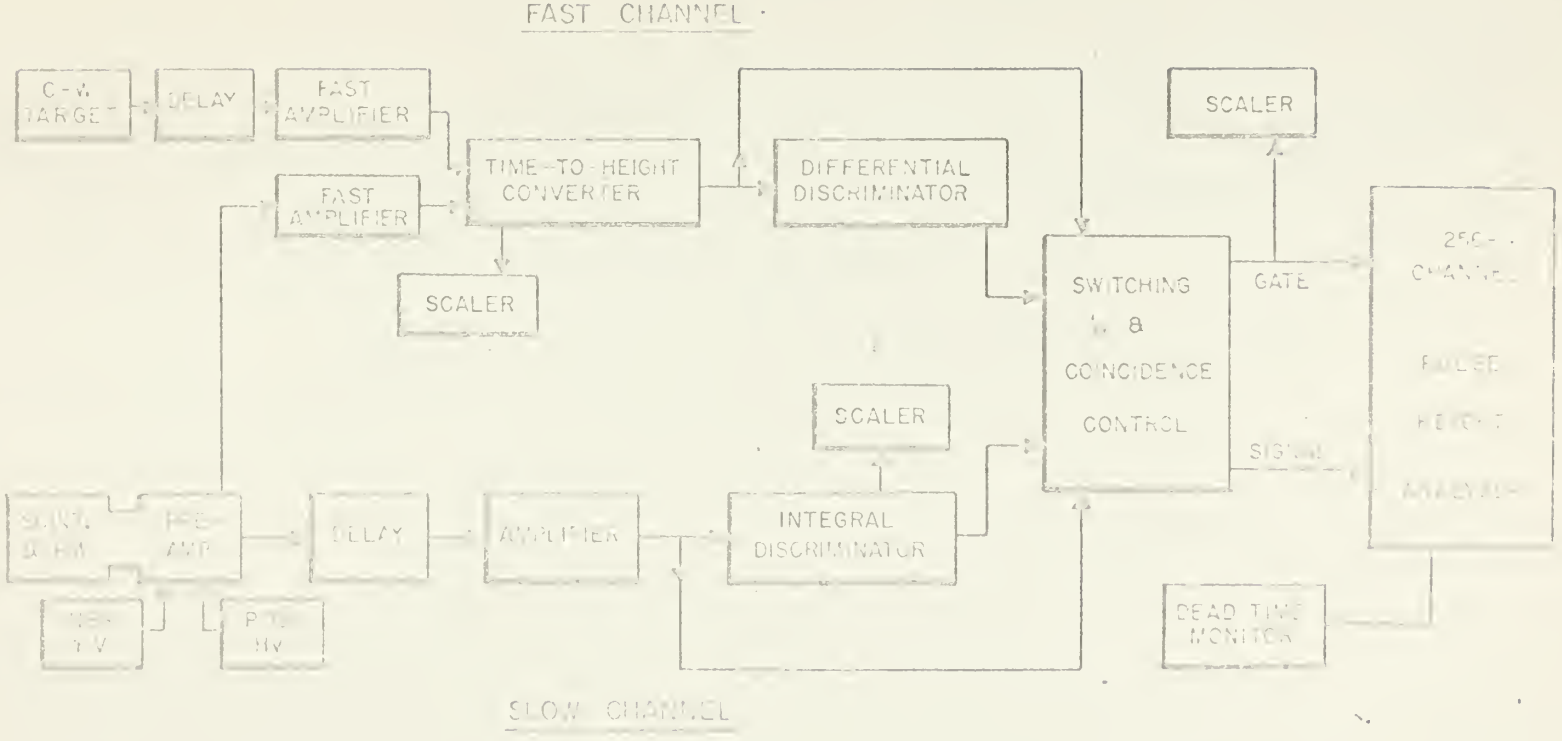

Fig. 4. Block diagram of detector-analyzer system.


PRE-AMP
ASSEMBLY
HOUSING
& CRYSTAL
COPPER
ATTENUATOR
TRITIUM
TARGET
ALPHA
COUNTER
SAND MATRIX

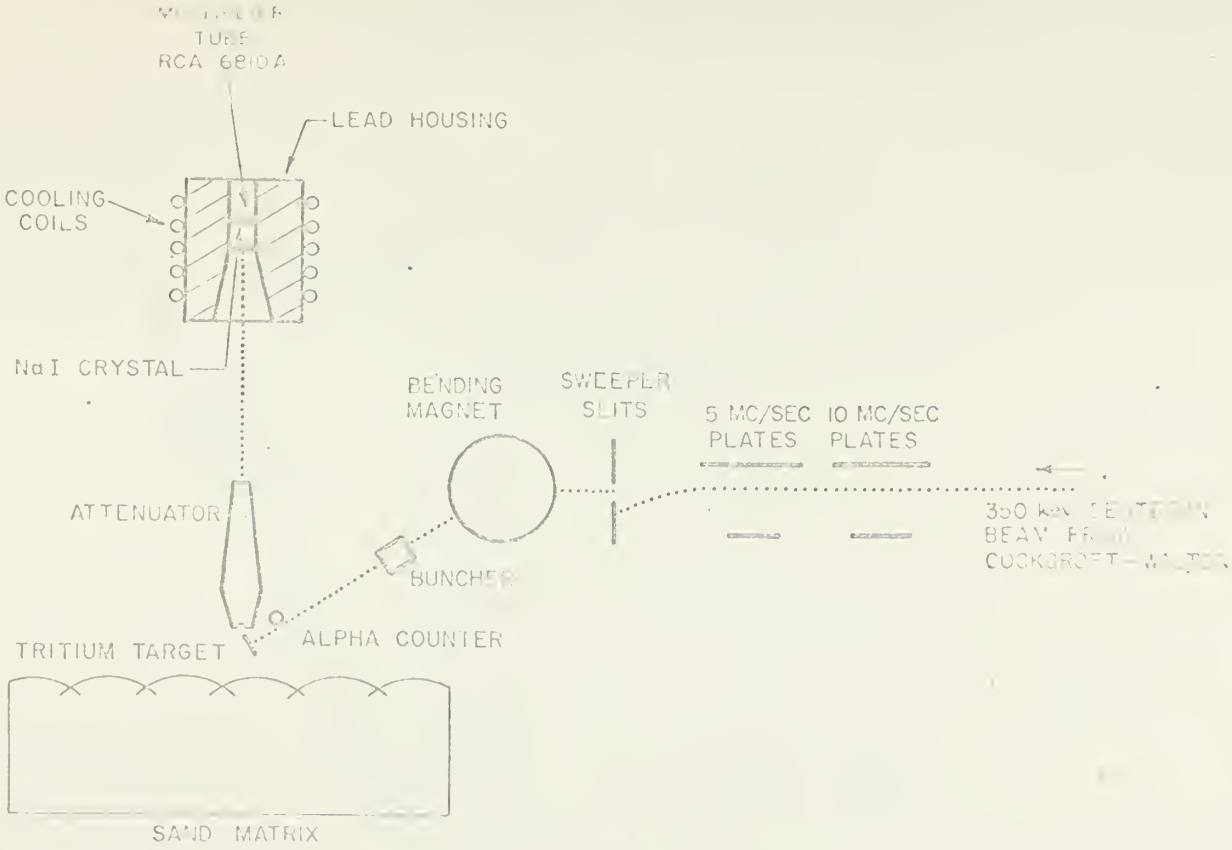

Fig. 6. Block diagram of "Formation" experiment.

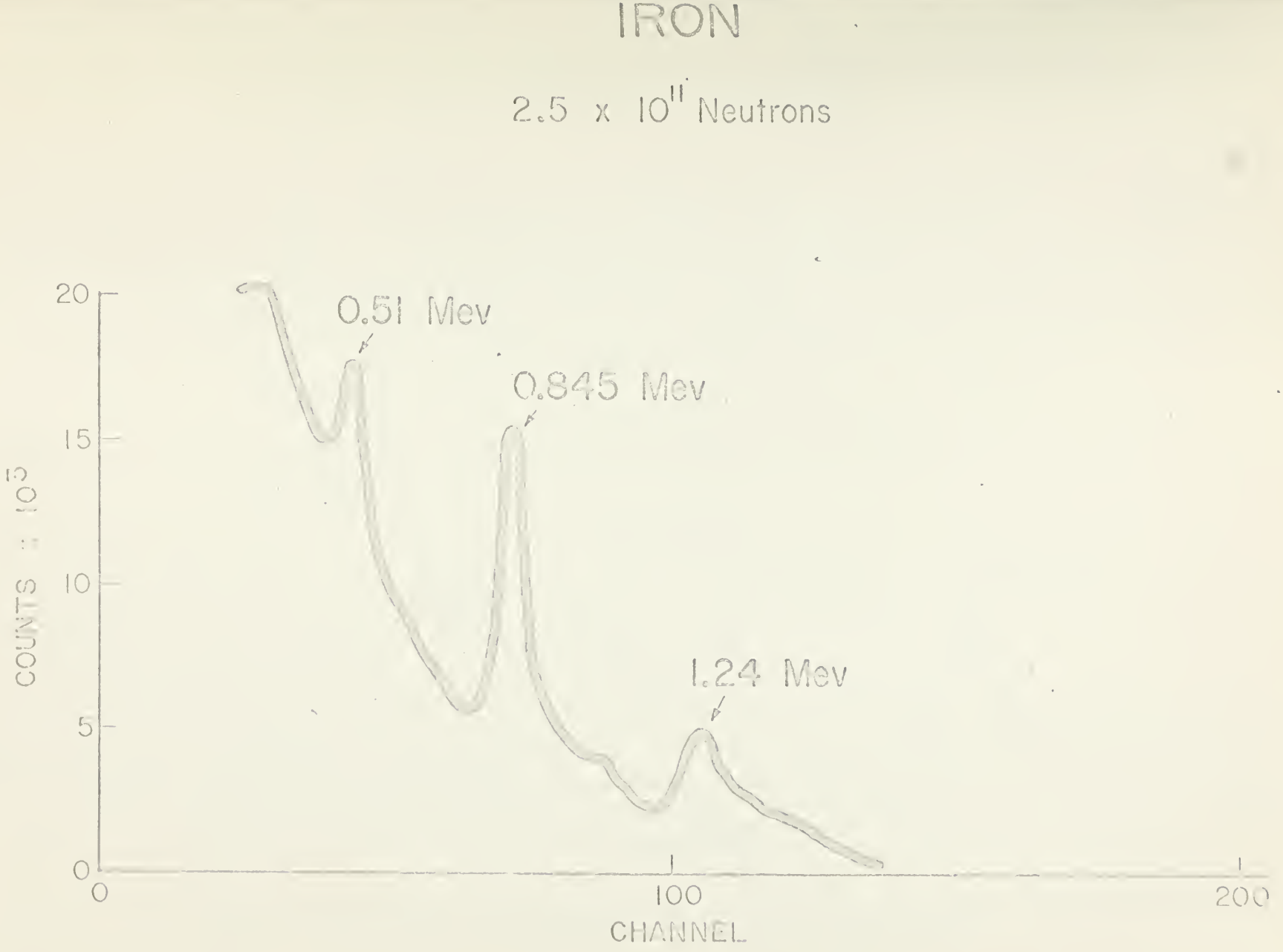

Fig. 7. Pulse height distribution from Iron. E_n = 14.3 Mev.

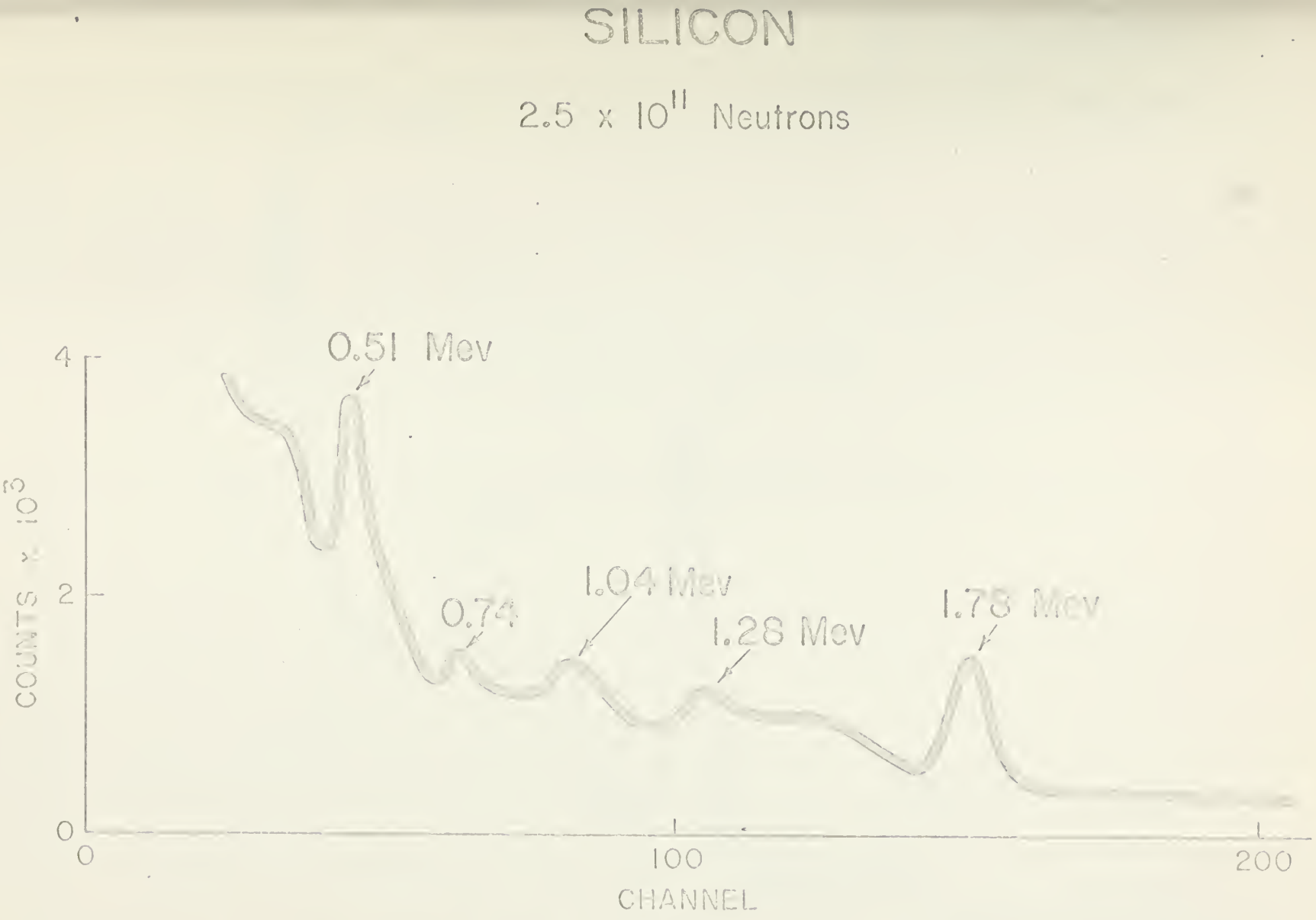

Fig. 8. Pulse height distribution from Silicon. E_n = 14.3 Mev.

Fig. 9. Pulse Height Distribution from Magnesium. E_n = 14.3 Mev.

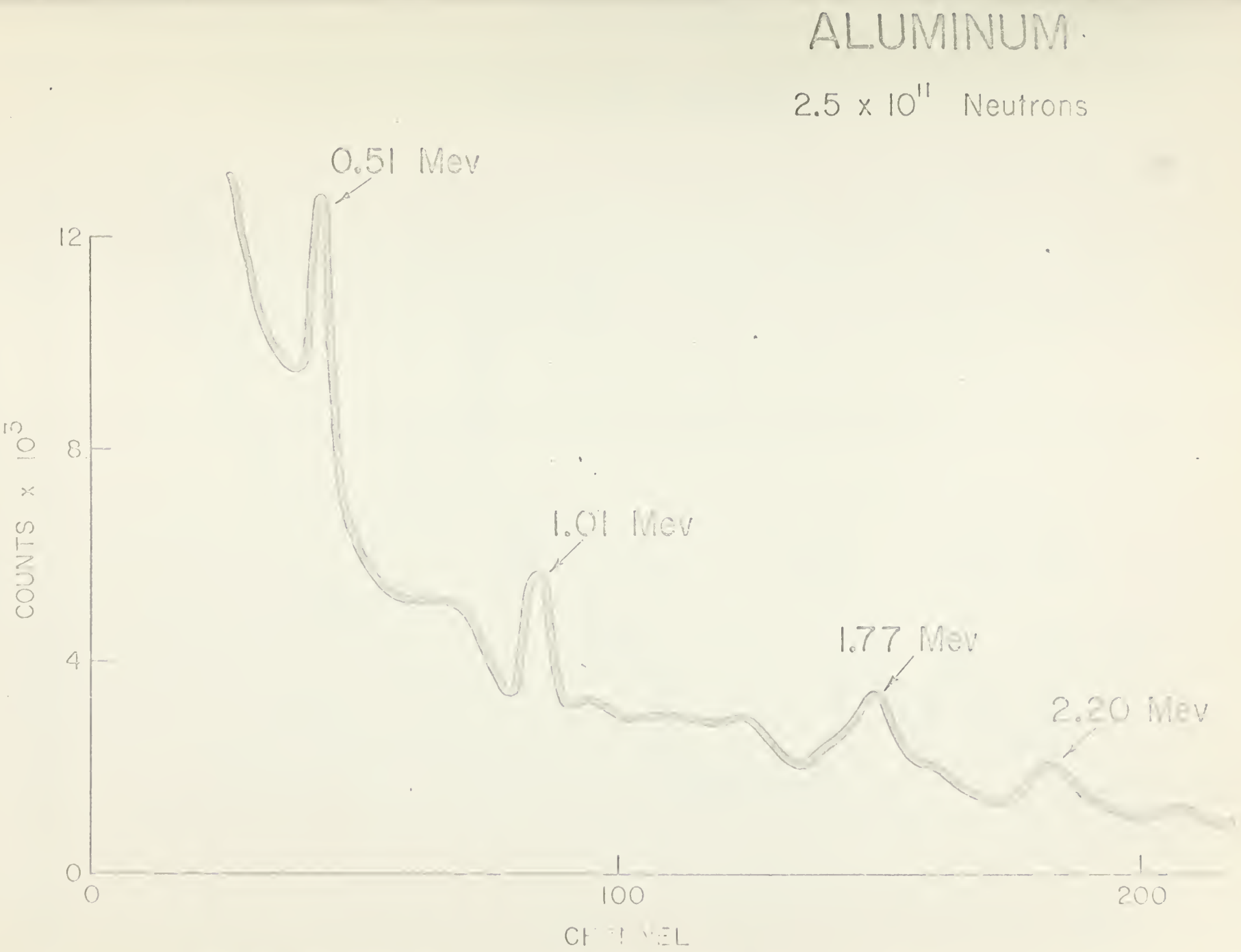

Fig. 10. Pulse height distribution from aluminum. E_n = 14.5 Mev.

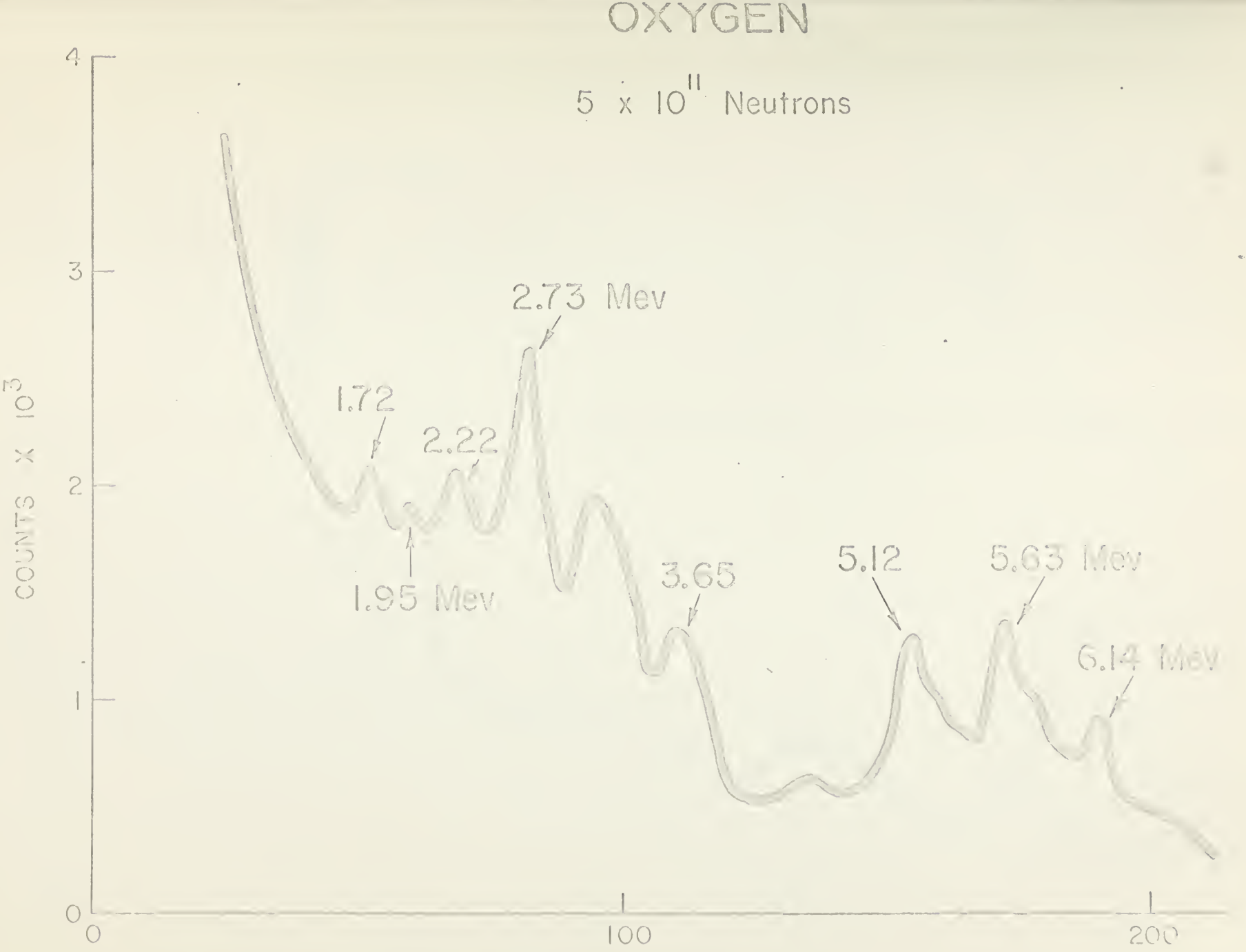
OXYGEN
5 x 10^11 Neutrons
COUNTS x 10^3
4
3
2
1
0
0
100
200
2.73 Mev
1.72
2.22
1.95 Mev
3.65
5.12
5.63 Mev
6.14 Mev

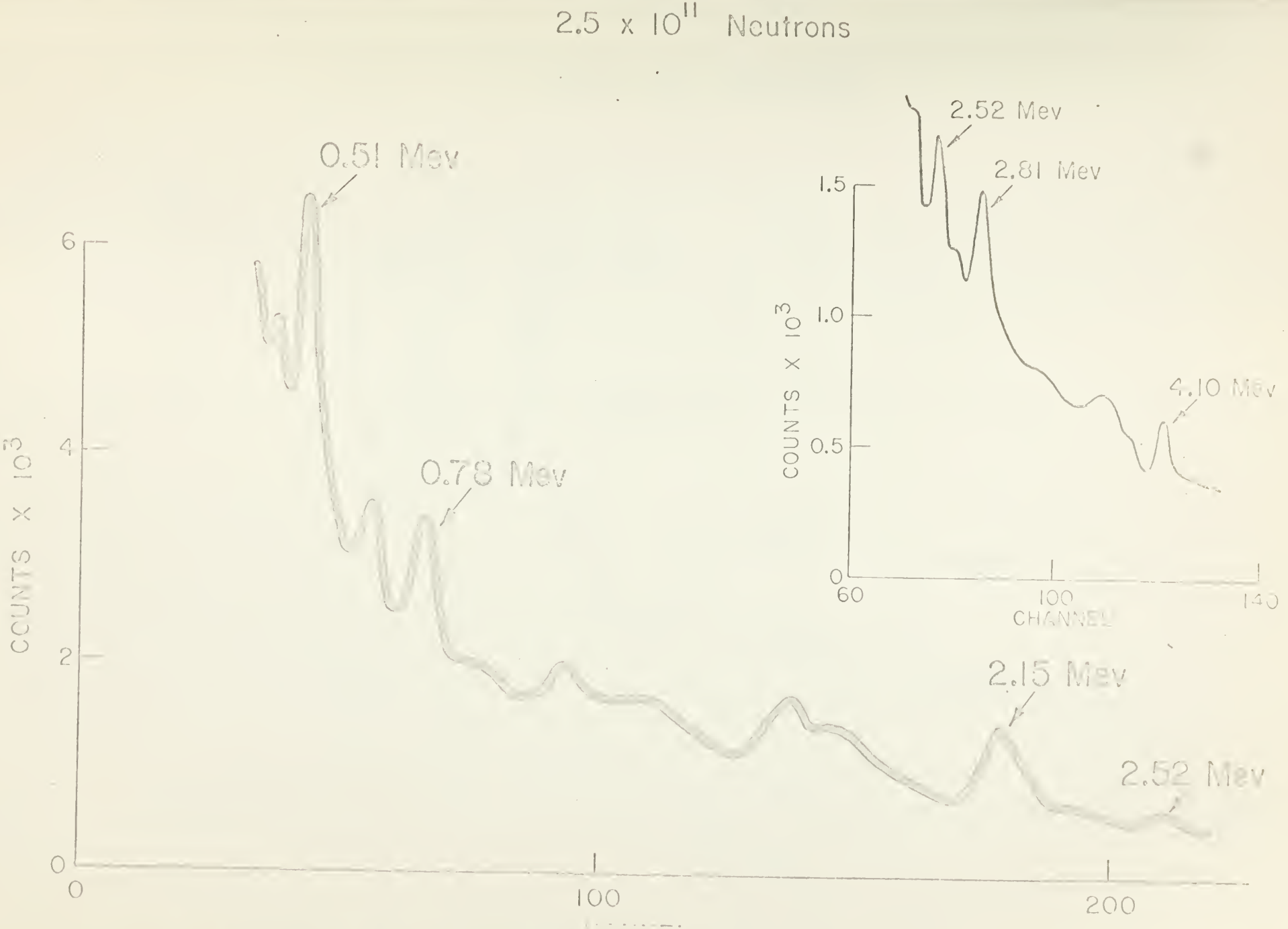

Fig. 19. Pulse height distribution from Polonium. E_n - 14.3 Mev.

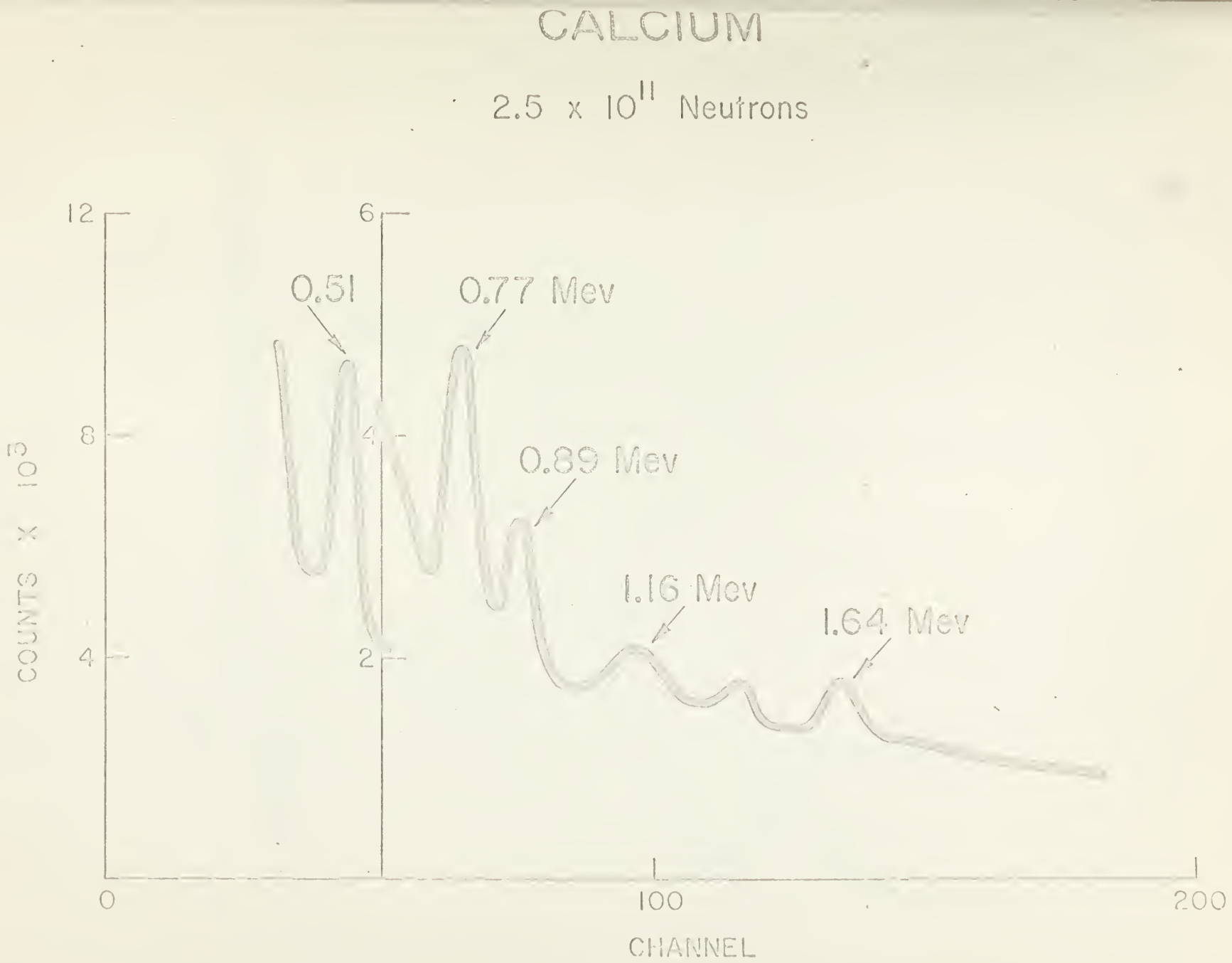

Fig. 14. Pulse height distribution from Calcium. E_n = 14.3 Mev.

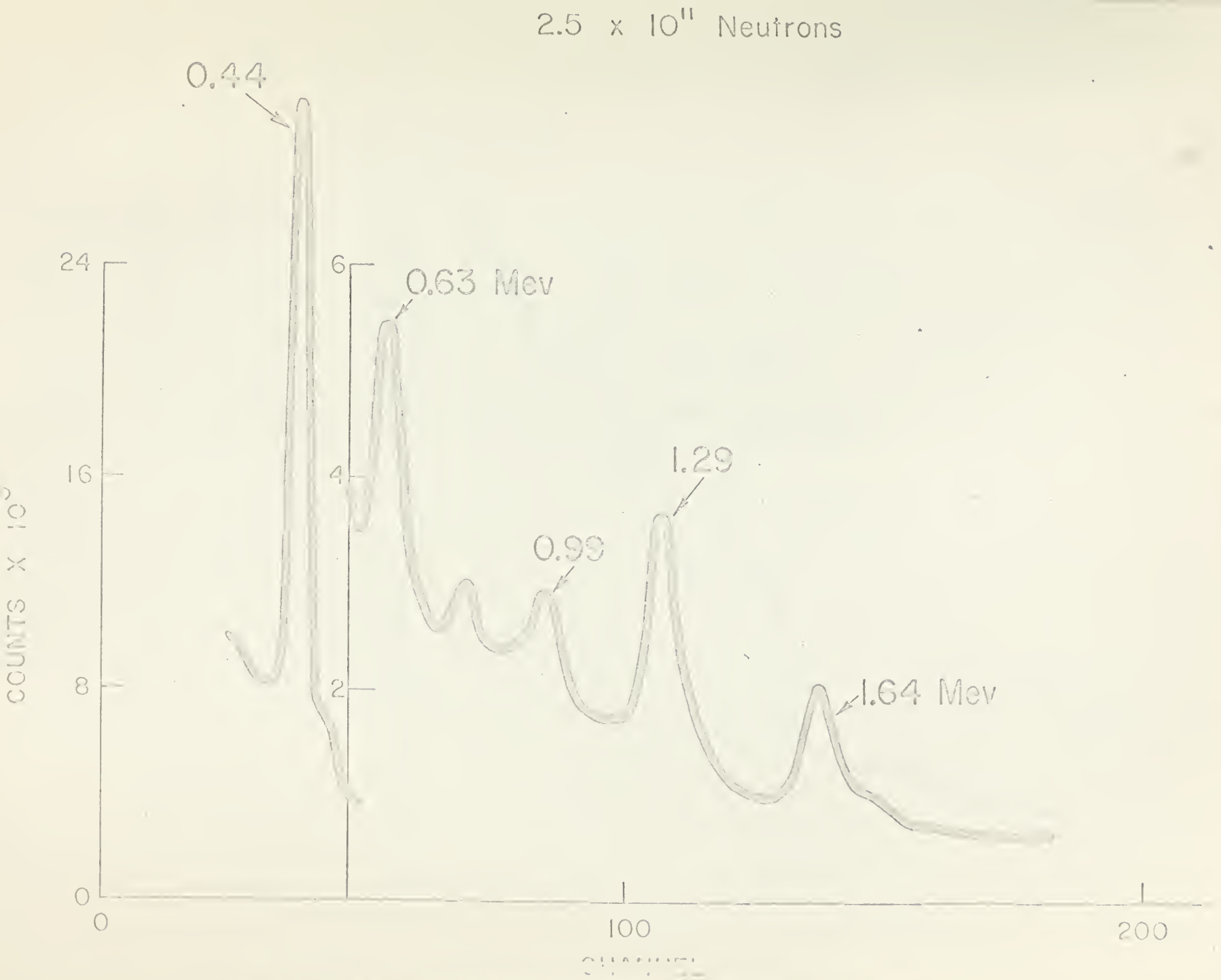

Fig. 21. Pulse height distribution from Boron. E_n = 14.3 Mev.

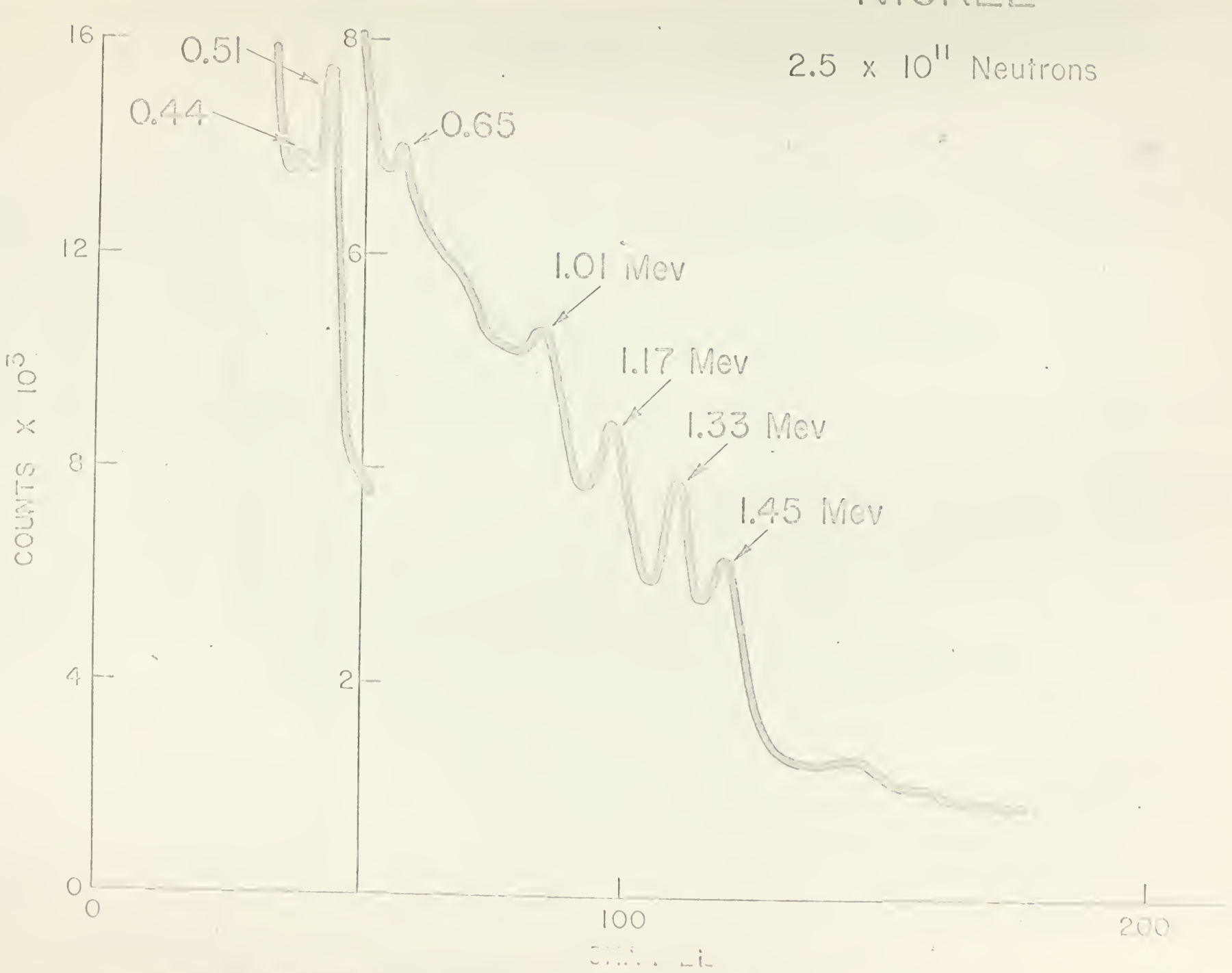
NICKEL
2.5 x 10^11 Neutrons
0.51
0.44
0.65
1.01 Mev
1.17 Mev
1.33 Mev
1.45 Mev
COUNTS x 10^3
16
12
8
4
0
8
6
2
0
100
200

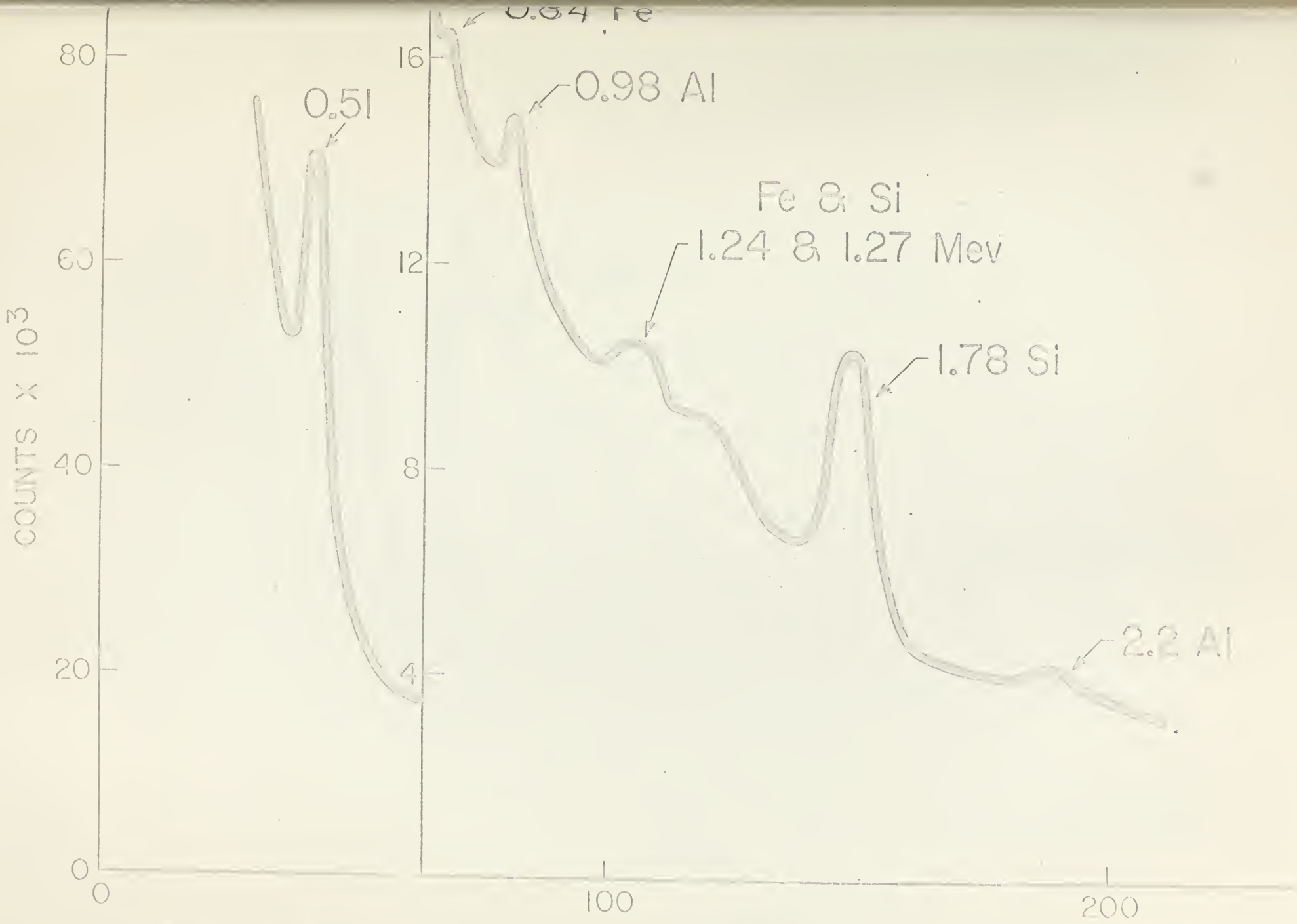

Fig. 16. Pulse height distribution
[illegible] vertically produced gamma rays from [illegible].

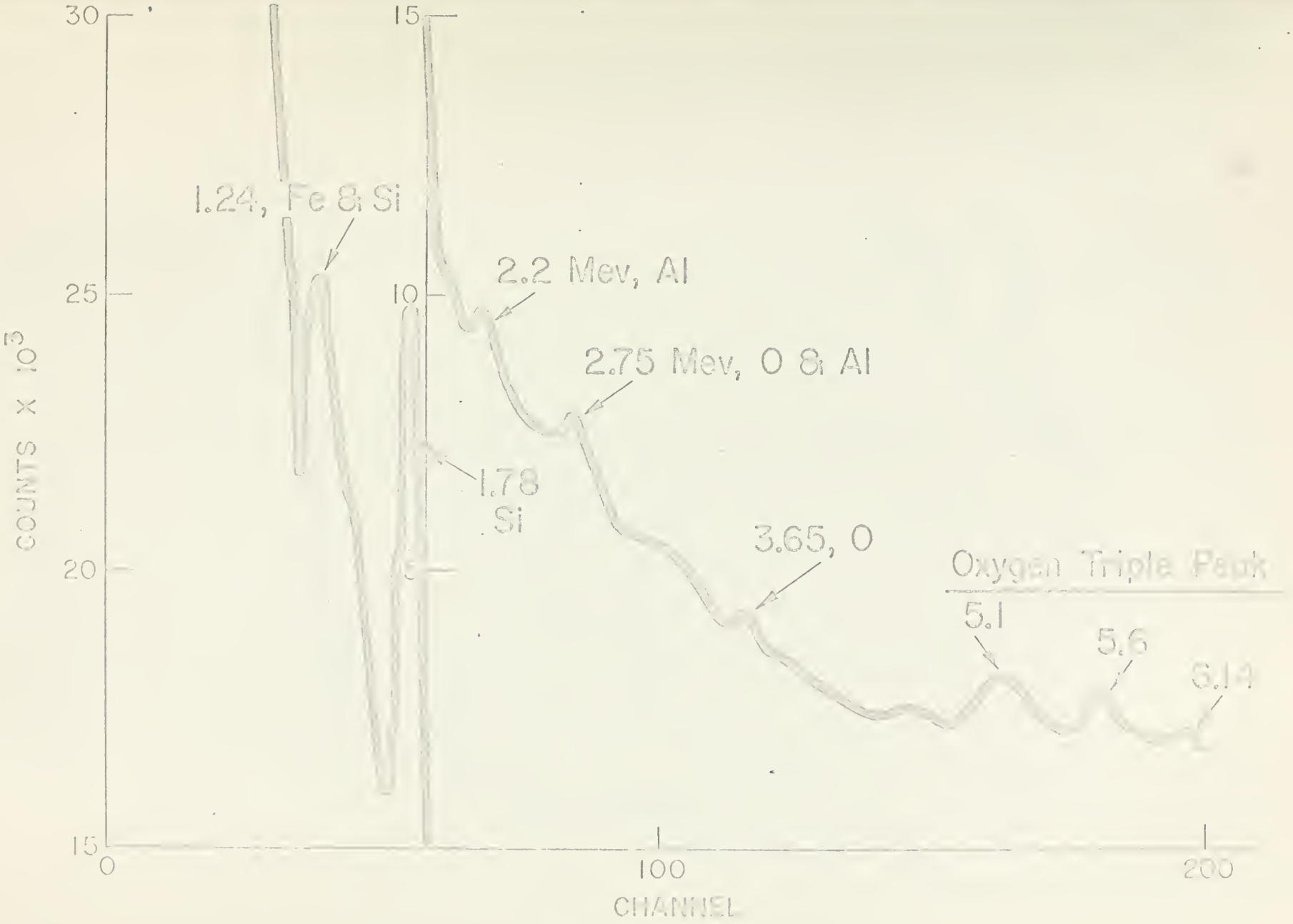

Fig. 17. Pulse height distribution from Samplic (0-8 Mev) E_n = 14.3 Mev.

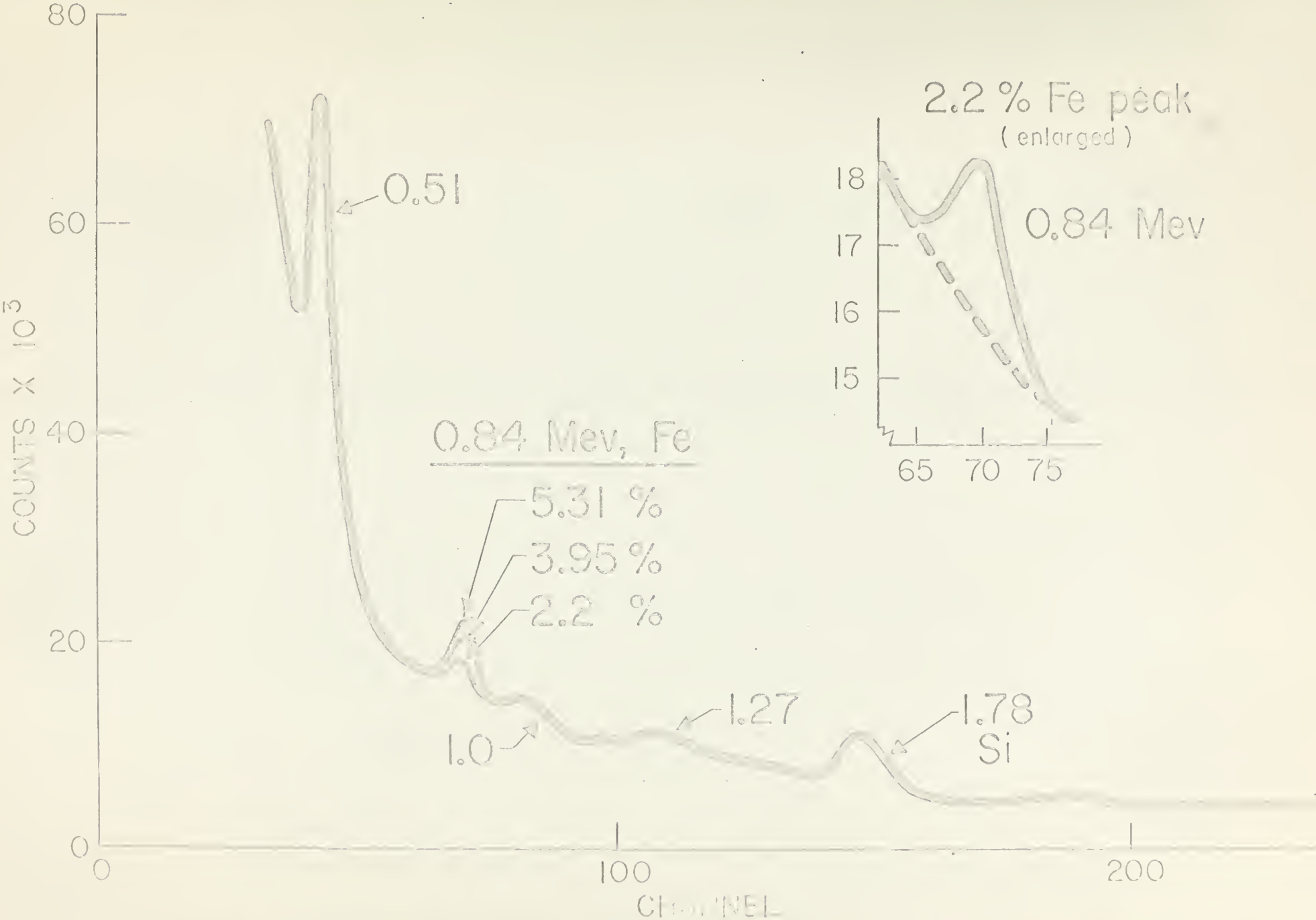

Fig. 3b. Pulse height distribution from Scintillo plus 2.2, 3.95, and 5.31% Fe by mass.

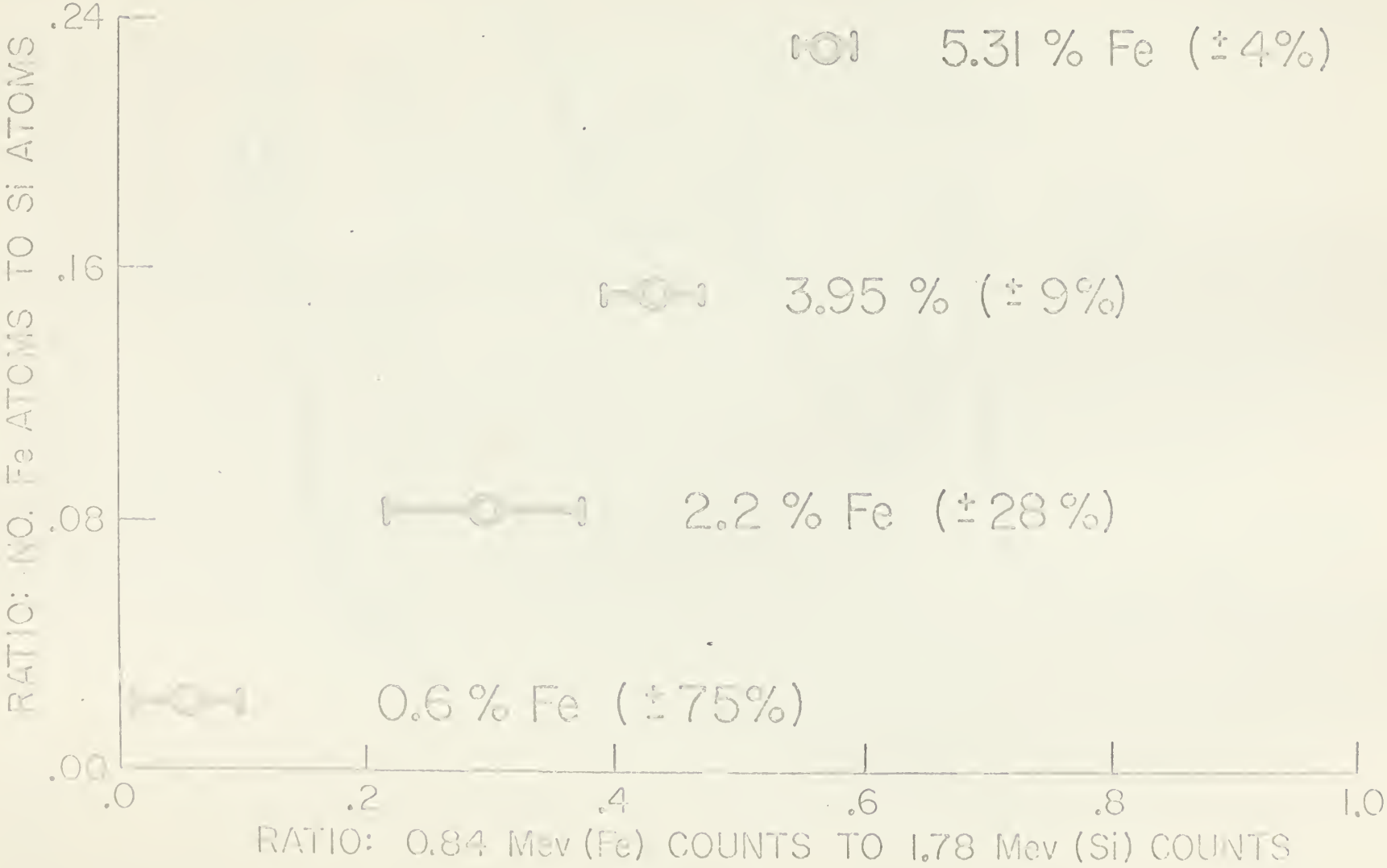

Fig. 19. Sensitivity and calibration curve for Fe.

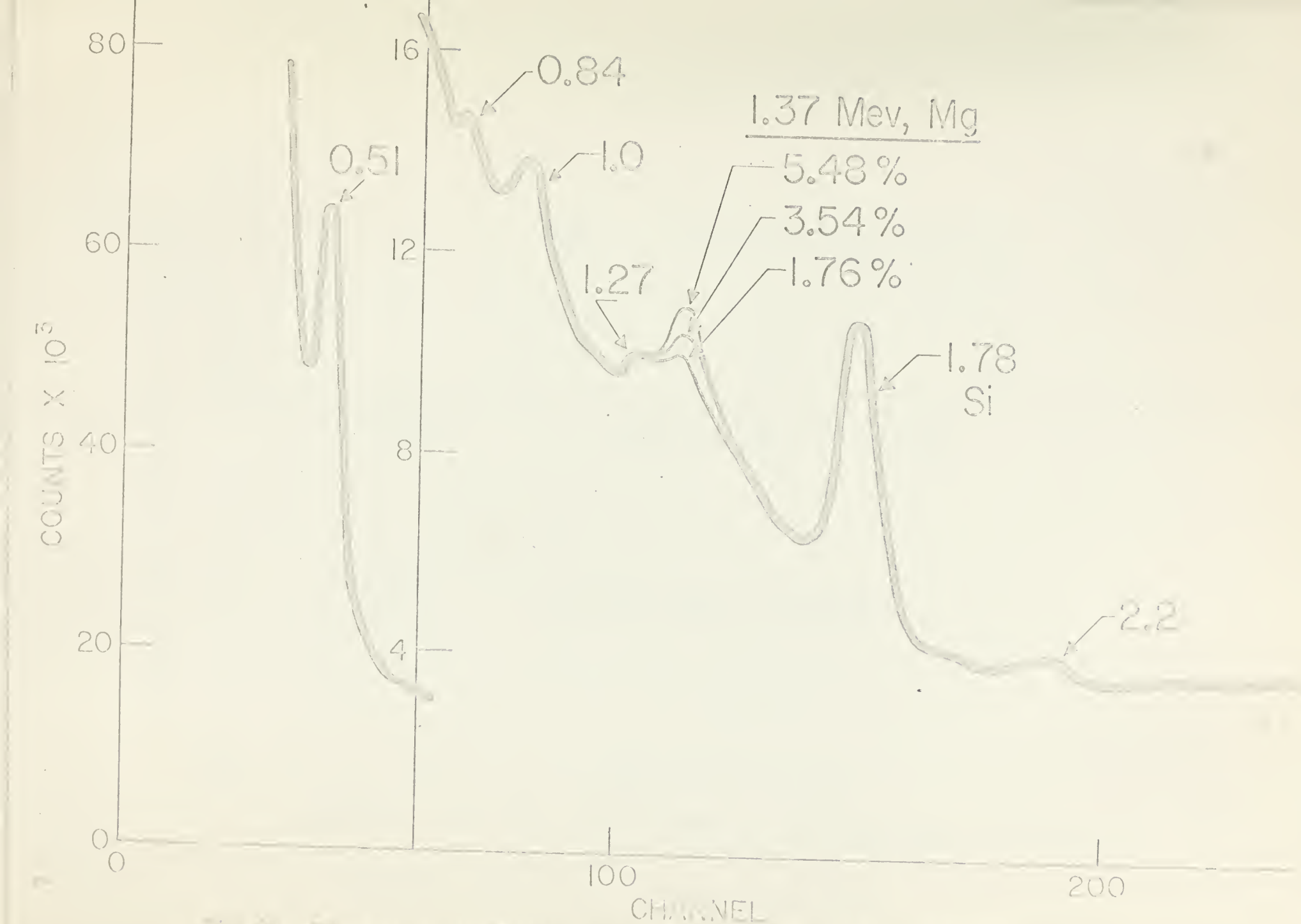
80
60
40
20
0
COUNTS X 10^3
16
12
8
4
0
0.84
0.51
1.0
1.27
1.37 Mev, Mg
5.48 %
3.54 %
1.76 %
1.78
Si
2.2
100
200
CHANNEL

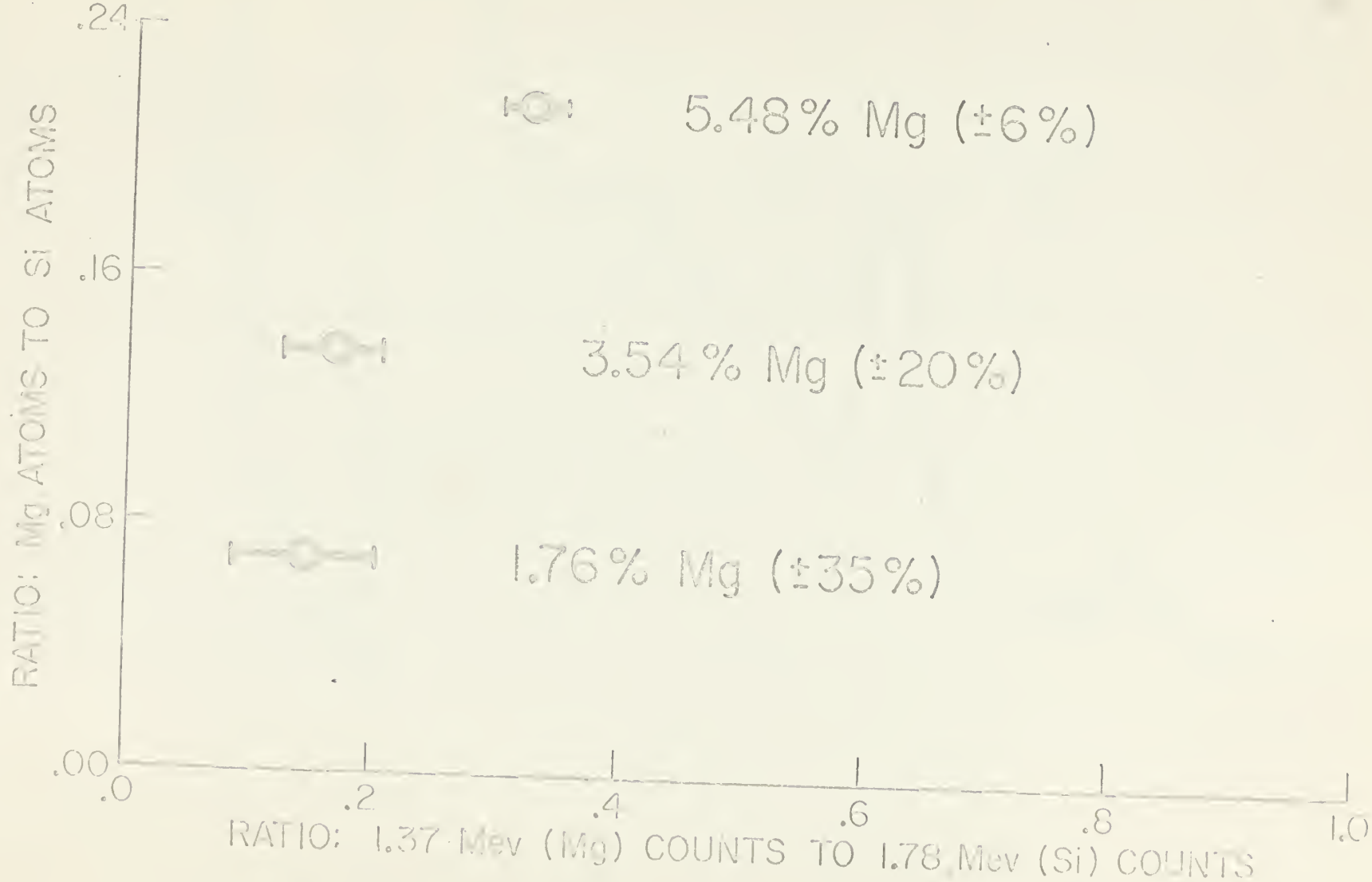

Fig. 21. Sensitivity and calibration curve for Mg.

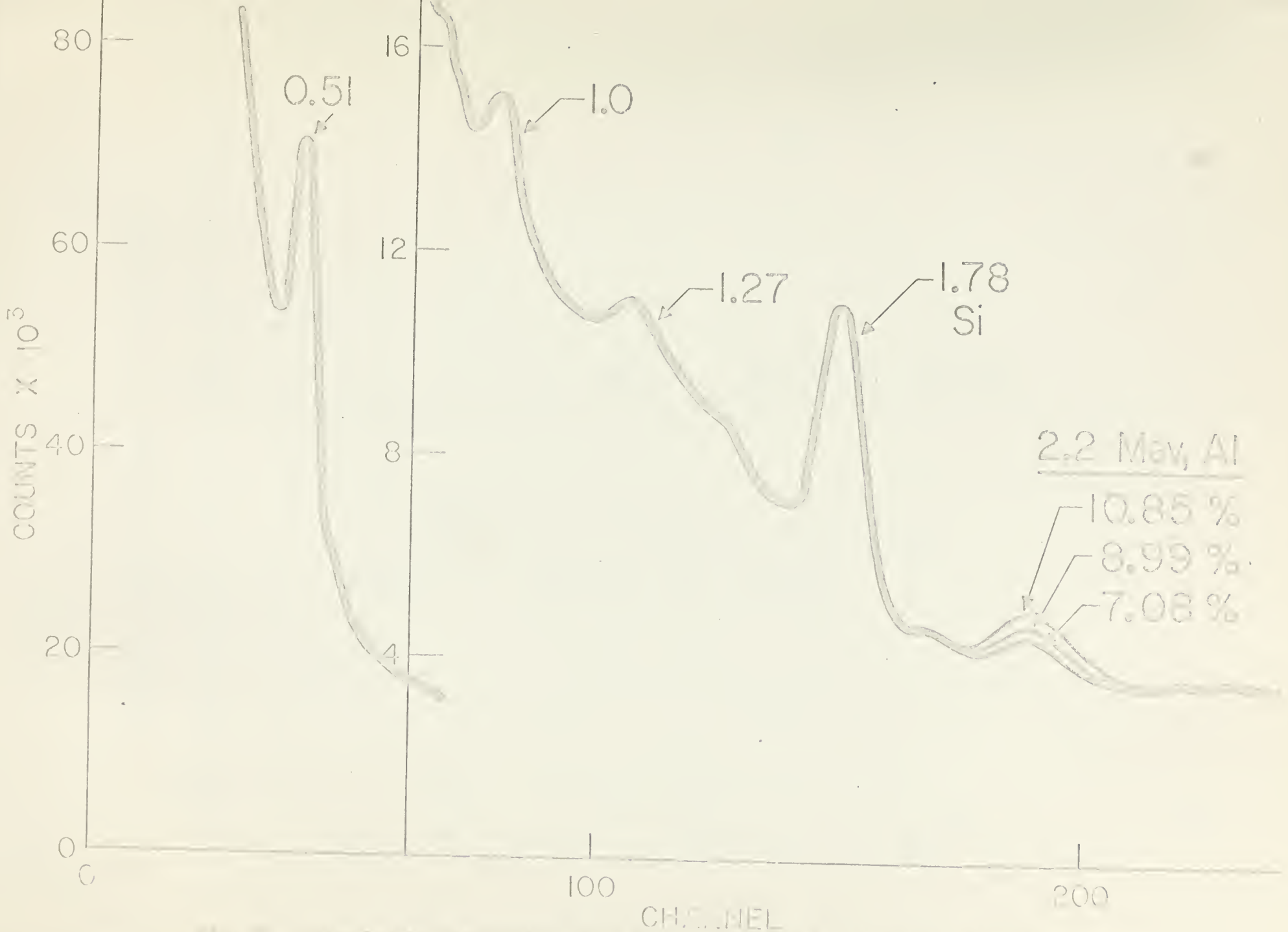
80
60
40
20
0
16
12
8
4
0.51
1.0
1.27
1.78
Si
2.2 Mev, Al
10.85 %
8.99 %
7.08 %
COUNTS X 10³
0
100
200
CHANNEL

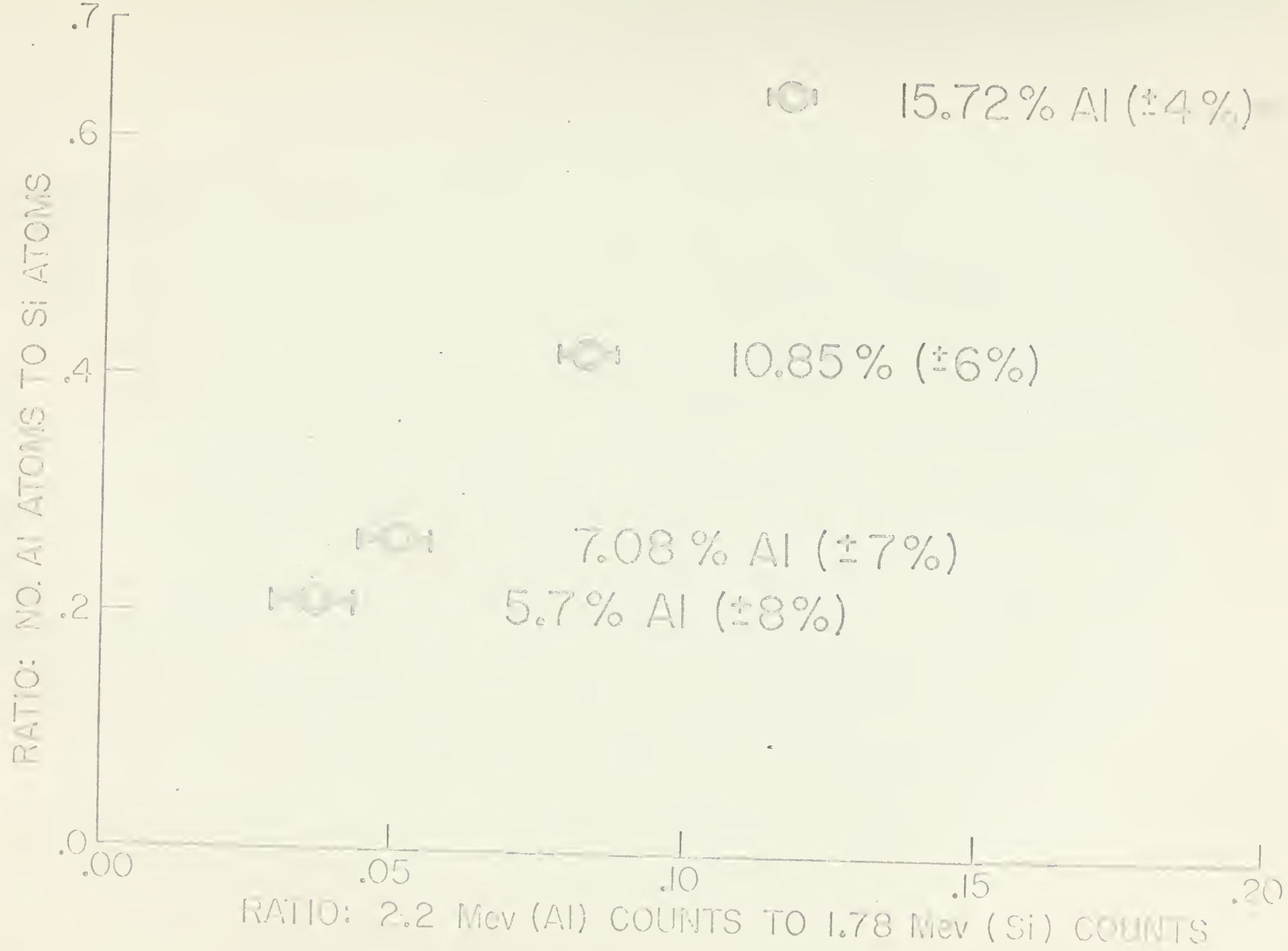

Fig. 21. Standardization calibration curve for Al.